

1 **Trans-Pacific transport and evolution of aerosols: Evaluation of quasi-**  
2 **global WRF-Chem simulation with multiple observations**

3 <sup>1,2</sup>Zhiyuan Hu, <sup>2</sup>Chun Zhao, <sup>1</sup>Jianping Huang, <sup>2</sup>L. Ruby Leung, <sup>2</sup>Yun Qian, <sup>3,4</sup>Hongbin  
4 Yu, <sup>5</sup>Lei Huang, <sup>5</sup>Olga V. Kalashnikova

5  
6 <sup>1</sup>Key Laboratory for Semi-Arid Climate Change of the Ministry of Education, Lanzhou  
7 University, Gansu, China

8 <sup>2</sup>Atmospheric Sciences and Global Change Division, Pacific Northwest National  
9 Laboratory, Richland, WA, USA

10 <sup>3</sup>Earth System Science Interdisciplinary Center, University of Maryland, MD, USA

11 <sup>4</sup>Earth Science Division, NASA Goddard Space Flight Center, MD, USA

12 <sup>5</sup>Jet Propulsion Laboratory, California Institute of Technology and NASA, Pasadena, CA,  
13 USA

14

15

16

17 Manuscript for submission to *WRF-Chem special issue in Geosci. Model Dev.*

18

19

20 \*Corresponding authors:

21 Chun Zhao, phone: (509) 371-6372; email: [chun.zhao@pnnl.gov](mailto:chun.zhao@pnnl.gov)

22

## 23 **Abstract**

24 A fully coupled meteorology-chemistry model (WRF-Chem, the Weather  
25 Research and Forecasting model coupled with chemistry) has been configured to conduct  
26 quasi-global simulation for the 5 years of 2010-2014 and evaluated with multiple  
27 observation datasets for the first time. The evaluation focuses on the simulation over the  
28 trans-Pacific transport region using various reanalysis and observational datasets for  
29 meteorological fields and aerosol properties. The simulation generally captures the  
30 overall spatial and seasonal variability of satellite retrieved aerosol optical depth (AOD)  
31 and absorbing AOD (AAOD) over the Pacific that is determined by the outflow of  
32 pollutants and dust and the emissions of marine aerosols. The assessment of simulated  
33 extinction Angstrom exponent (EAE) indicates that the model generally reproduces the  
34 variability of aerosol size distributions as seen by satellites. In addition, the vertical  
35 profile of aerosol extinction and its seasonality over the Pacific are also well simulated.  
36 The difference between the simulation and satellite retrievals can be mainly attributed to  
37 model biases in estimating marine aerosol emissions as well as the satellite sampling and  
38 retrieval uncertainties. Compared with the surface measurements over the western U.S.,  
39 the model reasonably simulates the observed magnitude and seasonality of dust, sulfate,  
40 and nitrate surface concentrations, but significantly underestimates the peak surface  
41 concentrations of carbonaceous aerosol likely due to model biases in the spatial and  
42 temporal variability of biomass burning emissions and secondary organic aerosol (SOA)  
43 production. A sensitivity simulation shows that the trans-Pacific transported dust, sulfate,  
44 and nitrate can make significant contribution to surface concentrations over the rural  
45 areas of the western U.S., while the peaks of carbonaceous aerosol surface concentrations

46 are dominated by the North American emissions. Both the retrievals and simulation show  
47 small interannual variability of aerosol characteristics for 2010-2014 averaged over three  
48 Pacific sub-regions. The evaluation in this study demonstrates that the WRF-Chem quasi-  
49 global simulation can be used for investigating trans-Pacific transport of aerosols and  
50 providing reasonable inflow chemical boundaries for the western U.S. to further  
51 understand the impact of transported pollutants on the regional air quality and climate  
52 with high-resolution nested regional modeling.

53

54

## 55 **1 Introduction**

56 Aerosols, including from natural and anthropogenic sources in Europe, North  
57 Africa, and East Asia, can be transported across the Pacific Ocean thousands of miles  
58 downwind to North America and even beyond. Previous studies using ground-based and  
59 satellite measurements and numerical models have estimated about 7-10 days of travel  
60 time for aerosols to traverse the Pacific Ocean (Eguchi et al., 2009). Previous studies  
61 have shown that aerosols outflowed from the Asian continent could be transported by the  
62 mid-latitude prevailing westerlies across the Pacific Ocean and ultimately reach the west  
63 coast of North America and beyond, and its efficiency is the largest in spring (e.g.,  
64 Takemura et al., 2002; Chin et al., 2007; Huang et al., 2008; Yu et al., 2008; Uno et al.,  
65 2009, 2011; Alizadeh-Choobari et al., 2014). Takemura et al. (2002) found that the  
66 contribution of anthropogenic aerosols to the total aerosol optical thickness is comparable  
67 to that of dust during the transport over the North Pacific in spring. Chin et al. (2007)  
68 found that the long-range transported dust brought 3 to 4 times more fine particles than  
69 anthropogenic pollutants to the total surface fine particles over the U.S. on annual  
70 average with a maximum influence in spring and over the northwestern U.S. Yu et al.  
71 (2008) estimated that about 25% of the Asian outflow reaches the west coast of North  
72 America, which is about 15% of the total North American emissions, and the transport  
73 fluxes are largest in spring and smallest in summer. Uno et al. (2011) also revealed that  
74 the dust trans-Pacific path sometimes could be split into two branches: a southern path to  
75 the central U.S. and a northern path that is trapped and stagnant for a longer time and  
76 finally subsides over the northwestern U.S.

77           These trans-Pacific aerosols can play an important role in atmospheric  
78 composition (e.g., Yu et al., 2008), air quality (e.g., Jaffe et al., 1999; VanCuren, 2003;  
79 Heald et al., 2006; Chin et al., 2007; Fischer et al., 2009; Yu et al., 2012; Tao et al.,  
80 2016), and regional weather and climate (e.g., Lau et al., 2008; Eguchi et al., 2009; Yu et  
81 al., 2012; Creamean et al., 2013; Fan et al., 2014; Huang et al., 2006, 2014) over the U.S.  
82 West Coast. At the surface, Heald et al. (2006) found that Asian anthropogenic aerosol  
83 plume increased aerosol concentrations in elevated regions of the northwestern U.S. by  
84  $0.16 \mu\text{g m}^{-3}$  in spring 2001. Chin et al. (2007) also found that long-range transported dust  
85 increased the annual mean fine particle concentrations by  $0.5\text{-}0.8 \mu\text{g m}^{-3}$  over the western  
86 U.S., with a maximum enhancement in spring. The trans-Pacific transported aerosols can  
87 also significantly absorb and scatter solar radiation (Yu et al., 2012; Fast et al., 2014; Tao  
88 et al., 2016), and serve as cloud condensation nuclei and ice nuclei that affect winter  
89 storms in the western U.S. (Sassen, 2002; Ault et al., 2011; Creamean et al., 2013; Fan et  
90 al., 2014). Deposition of the transported aerosols on/into snowpack in elevated regions  
91 (Hadley et al., 2010) may also accelerate snowmelt and influence the regional  
92 hydrological cycle and climate over the western U.S. (Qian et al., 2009 and 2015; Painter  
93 et al., 2010). Hence it is important to quantify the trans-Pacific transport of aerosols and  
94 how they evolve over the long distance.

95           Previous studies have used global models to quantify the long-range transport of  
96 aerosols to the western U.S. (e.g., Fairlie et al., 2007; Heald et al., 2006; Chin et al.,  
97 2007; Hadley et al., 2007). However, simulations were performed at relatively coarse  
98 resolutions (typically 1-2 degrees) that cannot fully resolve the large geographical  
99 variability of aerosols over the western U.S. with complex topography (Zhao et al.,

100 2013a). Coarse resolution simulations also lack the capability to fully resolve aerosol-  
101 cloud-precipitation interaction. Some studies have reported regional simulations at  
102 relatively high resolutions over the western U.S. (e.g., Zhao et al., 2013a; Fan et al.,  
103 2014; Fast et al., 2014). However, most of them either used sparse in-situ observations to  
104 provide lateral boundary conditions that are only suitable for idealized or short-term  
105 sensitivity studies, or used simulations from global models with inconsistent physics and  
106 chemistry schemes to provide lateral boundary conditions, which introduce biases in  
107 estimating the contribution and effect of trans-Pacific transported aerosols.

108 To investigate the impact of trans-Pacific transported aerosols on regional air  
109 quality and climate of the U.S. West Coast, a multi-scale modeling framework including  
110 global simulation at coarse resolutions that captures the large-scale circulation and  
111 provides consistent chemical lateral boundaries for nested regional simulation at high  
112 resolutions is needed. WRF-Chem, the Weather Research and Forecasting (WRF) model  
113 (Skamarock et al., 2008) coupled with a chemistry component (Grell et al., 2005), is such  
114 a modeling framework. As a state-of-the-art model, WRF-Chem supports nested  
115 simulations, and includes complex aerosol processes and interactions between aerosols  
116 and radiation, clouds, and snow albedo (Zhao et al., 2014). The model has been used  
117 extensively to study aerosols and their impacts on air quality and climate at regional  
118 scales (e.g., Fast et al., 2006, 2009; Gustafson et al., 2007; Qian et al., 2010; Gao et al.,  
119 2011, 2014; Shrivastava et al., 2011; Chen et al., 2013, 2014; Zhao et al., 2010, 2011,  
120 2012, 2013a; 2014). Zhao et al. (2013b) is the first study to use WRF-Chem for quasi-  
121 global (180° W-180° E, 60° S-70° N) simulations at a resolution of 1° × 1° to examine  
122 uncertainties in simulating global dust mass balance and radiative forcing.

123           Although the quasi-global WRF-Chem simulation described by Zhao et al. (2013b)  
124 has been used to provide realistic chemical lateral boundary conditions for multiple  
125 regional modeling studies (e.g., Zhao et al., 2014; Fan et al., 2015), its evaluation has not  
126 been documented so far. In this study, the WRF-Chem simulation for 2010-2014 is  
127 evaluated extensively using observational data. For lack of in-situ observations over East  
128 Asia and the Pacific Ocean during our simulation period, evaluation is performed mainly  
129 using reanalysis and satellite retrieval (e.g., CALISPO, MODIS, and MISR) datasets,  
130 along with some available ground-based observations from AERONET and IMPROVE  
131 in the region. We focus on the simulation over the trans-Pacific transport region as a first  
132 step to evaluate the simulation for providing consistent lateral chemical boundaries for  
133 nested regional simulations used to investigate the impact of transported aerosols on  
134 regional air quality and climate. Spatial evolution of aerosols during the trans-Pacific  
135 transport as well as their seasonal and annual variability simulated by WRF-Chem will  
136 also be characterized.

137           In the following sections, the detailed setup of WRF-Chem will be described in  
138 Section 2. In Section 3 ground-based measurements and satellite retrievals will be  
139 presented. In Section 4, we evaluate the WRF-Chem simulated spatial distributions and  
140 seasonal and annual variability of aerosols across the Pacific with the observations. The  
141 conclusion can be found in Section 5.

142

## 143 **2 Model description**

### 144 **2.1 WRF-Chem**

145 In this study, WRF-Chem (3.5.1), updated by scientists at Pacific Northwest  
146 National Laboratory (PNNL), is used. The MOSAIC (Model for Simulation Aerosol  
147 Interactions and Chemistry) aerosol module (Zaveri et al., 2008) coupled with the CBM-  
148 Z (carbon bond mechanism) photochemical mechanism (Zaveri and Peters, 1999) in  
149 WRF-Chem is selected in this study. MOSAIC uses a sectional approach to represent  
150 aerosol size distributions with four or eight discrete size bins in the current version of  
151 WRF-Chem (Fast et al., 2006). All major aerosol components including sulfate ( $\text{SO}_4^{2-}$ ),  
152 nitrate ( $\text{NO}_3^-$ ), ammonium ( $\text{NH}_4^+$ ), black carbon (BC), organic matter (OM), sea-salt, and  
153 mineral dust are simulated in the model. The MOSAIC aerosol scheme includes physical  
154 and chemical processes of nucleation, condensation, coagulation, aqueous phase  
155 chemistry, and water uptake by aerosols. Dry deposition of aerosol mass and number is  
156 simulated following the approach of Binkowski and Shankar (1995), which includes both  
157 turbulent diffusion and gravitational settling. Wet removal of aerosols by grid-resolved  
158 stratiform clouds and precipitation includes in-cloud removal (rainout) and below-cloud  
159 removal (washout) by impaction and interception, following Easter et al. (2004) and  
160 Chapman et al. (2009). Cloud-ice-borne aerosols through ice nucleation of aerosols are  
161 not considered in the model, but the removal of aerosols by the droplet freezing process is  
162 considered. Convective transport and wet removal of aerosols by cumulus clouds follow  
163 Zhao et al. (2013b).

164 Aerosol optical properties such as extinction, single scattering albedo (SSA), and  
165 asymmetry factor for scattering are computed as a function of wavelength for each model  
166 grid box. Aerosols are assumed internally mixed in each bin (i.e., a complex refractive  
167 index is calculated by volume averaging for each bin for each chemical constituent of

168 aerosols). The Optical Properties of Aerosols and Clouds (OPAC) data set (Hess et al.,  
169 1998) is used for the shortwave (SW) and longwave (LW) refractive indices of aerosols,  
170 except that a constant value of  $1.53+0.003i$  is used for the SW refractive index of dust  
171 following Zhao et al. (2010, 2011). A detailed description of the computation of aerosol  
172 optical properties in WRF-Chem can be found in Fast et al. (2006) and Barnard et al.  
173 (2010). Aerosol radiative feedback is coupled with the Rapid Radiative Transfer Model  
174 (RRTMG) (Mlawer et al., 1997; Iacono et al., 2000) for both SW and LW radiation as  
175 implemented by Zhao et al. (2011). The optical properties and direct radiative forcing of  
176 individual aerosol species in the atmosphere are diagnosed following the methodology  
177 described in Zhao et al. (2013a). Aerosol-cloud interactions were included in the model  
178 by Gustafson et al. (2007) for calculating the activation and resuspension between dry  
179 aerosols and cloud droplets.

## 180 **2.2 Numerical experiments**

181       Following Zhao et al. (2013b), we use a quasi-global channel configuration with  
182 periodic boundary conditions in the zonal direction and  $360 \times 145$  grid cells ( $180^\circ$  W- $180^\circ$   
183 E,  $67.5^\circ$  S- $77.5^\circ$  N) to perform simulation at  $1^\circ$  horizontal resolution over the period  
184 2010-2014. Alizadeh-Choobari et al. (2015) conducted a global WRF-Chem simulation  
185 of dust and its radiative forcing, which was configured with dust aerosol only without  
186 other aerosols and chemistry. However, WRF-Chem global simulation with sophisticated  
187 chemistry including anthropogenic and natural aerosols could not run stably due  
188 potentially to convergence issue of solving chemical reactions near the relatively pristine  
189 polar regions. Given the need of sophisticated chemistry to simulate not only dust but  
190 also other anthropogenic aerosols, a more stable near global coverage WRF-Chem

191 configuration is used in this study to circumvent this technical difficulty to characterize  
192 the trans-Pacific transport of aerosols. The simulation is configured with 35 vertical  
193 layers up to 50 hPa. The meteorological initial and lateral meridional boundary  
194 conditions are derived from the National Center for Environmental Prediction final  
195 analysis (NCEP/FNL) data at 1° horizontal resolution and 6 h temporal intervals. The  
196 modeled wind components  $u$  and  $v$  and atmospheric temperature are nudged towards the  
197 NCEP/FNL reanalysis data throughout the domain with a nudging timescale of 6 h in all  
198 cases (Stauffer and Seaman, 1990). This provides a more realistic simulation of large-  
199 scale circulation, which is important for modeling long-range transport. The chemical  
200 initial and meridional boundary conditions are taken from the default profiles in WRF-  
201 Chem, which are the same as those used by McKeen et al. (2002) and are based on  
202 averages of mid-latitude aircraft profiles from several field studies over the eastern  
203 Pacific Ocean. The impact of chemical boundary conditions on the simulated results is  
204 negligible (Zhao et al. 2013b). This study uses a set of selected schemes for model  
205 physics, including the MYJ (Mellor–Yamada–Janjic) planetary boundary layer scheme,  
206 Noah land surface scheme, Morrison 2-moment microphysics scheme, Kain-Fritsch  
207 cumulus scheme, and RRTMG longwave and shortwave radiation schemes.

### 208 **2.3 Emissions**

209 Anthropogenic emissions are obtained from the REanalysis of the TROpospheric  
210 (RETRO) chemical composition inventories (<http://retro.enes.org/index.shtml>) except  
211 over East Asia and the United States. Over the U.S., the National Emission Inventory  
212 (NEI) 2011 is used. Over East Asia, the Asian emission inventory described by Zhang et  
213 al. (2009) at 0.5°x0.5° horizontal resolution for 2006 is used except that BC, OC, and

214 sulfate emissions over China are from the China emission inventory for 2010 described  
215 by Lu et al. (2011) at a  $0.1^\circ \times 0.1^\circ$  horizontal spatial resolution and a monthly temporal  
216 resolution for the simulation period. Biogenic emissions are calculated following  
217 Guenther et al. (1994). Biomass burning emissions are obtained from the Global Fire  
218 Emissions Database, Version 3 (GFEDv3) with monthly temporal resolution (van der  
219 Werf et al., 2010) and vertically distributed following the injection heights suggested by  
220 Dentener et al. (2006) for the Aerosol Comparison between Observations and Models  
221 (AeroCom) project. The WRF-Chem code is modified to update the biomass burning  
222 emissions every day. Sea-salt emission follows Zhao et al. (2013a), which is based on  
223 Gong (2003) to include correction of particles with radius less than  $0.2 \mu\text{m}$  and Jaegle et  
224 al. (2011) to include the sea-salt emission dependence on sea surface temperature.  
225 Vertical dust emission fluxes are calculated with the Goddard Chemical Aerosol  
226 Radiation Transport (GOCART) dust emission scheme (Ginoux et al., 2001), and the  
227 emitted dust particles are distributed into the MOSAIC aerosol size bins following a  
228 theoretical expression based on the physics of scale-invariant fragmentation of brittle  
229 materials derived by Kok (2011). For MOSAIC 8-bin, dust particles are emitted into  
230 eight size bins with mass fractions of  $10^{-6}\%$ ,  $10^{-4}\%$ ,  $0.02\%$ ,  $0.2\%$ ,  $1.5\%$ ,  $6\%$ ,  $26\%$ , and  
231  $45\%$ , respectively. Although the main purpose of this study is to evaluate the WRF-Chem  
232 simulation, a sensitivity simulation, in which dust, fire, and anthropogenic emissions over  
233 North America ( $10^\circ\text{N}$ - $70^\circ\text{N}$  and  $170^\circ\text{W}$ - $60^\circ\text{W}$ ) are removed, is also conducted to  
234 understand the contribution of trans-Pacific transported aerosols to the surface aerosol  
235 concentrations over the western U.S.  
236

237 **3 Aerosol Observations**

238 **3.1 Satellite Retrievals**

239 **3.1.1 MODIS**

240 The Moderate Resolution Imaging Spectroradiometer (MODIS) instrument  
241 onboard the NASA EOS Terra satellite observes Earth in 36 spectral bands from 0.4 to  
242 14.4  $\mu\text{m}$ , and provides nearly daily global coverage with local equatorial overpass time of  
243 about 10:30 AM since 2000 (King et al., 1999). The “dark target” algorithm has been  
244 developed to retrieve AOD and size parameters (Angstrom exponent, effective radius,  
245 and fine-mode fraction) over waters and vegetated lands (Kaufman et al., 1997; Remer et  
246 al., 2005). The “deep blue” algorithm has been implemented to retrieve AOD over bright  
247 land initially, which then has also been extended to vegetated land (Hsu et al., 2006,  
248 2013). MODIS aerosol products have been widely used to characterize the regional,  
249 seasonal, and global distribution of aerosol and its components (Yu et al., 2003, 2009;  
250 Chin et al., 2004; Kaufman et al., 2005a), estimate aerosol radiative forcing (Yu et al.,  
251 2004; Remer and Kaufman, 2006), and study aerosol-cloud interactions (Kaufman et al.,  
252 2005b; Koren et al., 2005; Yu et al., 2007). In this study, MODIS data from the collection  
253 5.1 are used. We use the “deep blue” AOD over land and the “dark target” AOD over  
254 ocean, both at 550 nm and at  $1^\circ \times 1^\circ$  horizontal resolution. Also, we use the “dark target”  
255 over-ocean extinction Angstrom exponent (EAE) over the 470-660 nm wavelength range  
256 to evaluate model simulations of particle size information (Anderson et al., 2005; Remer  
257 et al., 2005; Levy et al., 2013).

258 **3.1.2 MISR**

259           The Multi-angle Imaging SpectroRadiometer (MISR) instrument onboard the  
260 Terra spacecraft crosses the equator at ~10:30 AM local time since 1999. It observes  
261 continuously in four narrow spectral bands centered at 446, 558, 672 and 866 nm using  
262 nine separate cameras oriented along the orbital track with surface viewing zenith angles  
263 ranging from  $\pm 70.5^\circ$  (Diner et al., 1998). Aerosol retrievals are performed on  $16 \times 16$   
264 patches of 1.1 km sub-regions, yielding an aerosol product at  $17.6 \times 17.6$  km spatial  
265 resolution, referred to as a “Level 2” product (Martonchik et al., 2002). MISR Level 2  
266 aerosol products have been described in Kahn et al (2009). The latest version (Version 22)  
267 of MISR aerosol product also provides the fraction of AOD due to “fine” (particle radii  
268  $< 0.35 \mu\text{m}$ ), “medium” (particle radii between 0.35 and  $0.7 \mu\text{m}$ ) and “large” (particle  
269 radii  $> 0.7 \mu\text{m}$ ) particles as well as the fraction of AOD due to “spherical” and  
270 “nonspherical” particles at the four MISR spectral bands. Here, we compare the MISR  
271 AOD at 550 nm from Version 22 of Level 2 with the model results.

### 272 **3.1.3 OMI**

273           OMI onboard the NASA Aura satellite has a daily global coverage, and crosses  
274 the equator at 1:45 PM local time. The nadir horizontal resolution of OMI is  $24 \times 13 \text{ km}^2$ .  
275 In this study the OMAERUV Level 2 Collection 003 V1.4.2 product (Jethva et al., 2014)  
276 is used as an independent data set providing SSA that is derived based on the reflectances  
277 measured by the OMI instrument at  $0.39 \mu\text{m}$ . The information on aerosol absorption in  
278 OMI measurements comes, to a large extent, from the interaction with Rayleigh  
279 scattering in the UV spectral region (Torres et al., 2013). The retrieved parameters are  
280 also reported at  $0.38 \mu\text{m}$  and  $0.50 \mu\text{m}$ . Current OMI AOD has positive biases likely due  
281 to a combination of factors including cloud contamination, surface albedo effects,

282 radiometric calibrations, and misidentified aerosol type (Ahn et al., 2008). Therefore, in  
283 this study, OMI AAOD at 500 nm is reconstructed using the WRF-Chem simulated 500  
284 nm AOD and OMI SSA at 500 nm with the formula of  $AAOD_{OMI}=AOD_{MODEL}\times(1-$   
285  $SSA_{OMI})$ .

#### 286 **3.1.4 CALIPSO**

287 In this study, we use aerosol extinction profiles retrieved by the Cloud-Aerosol  
288 Lidar with Orthogonal Polarization (CALIOP) onboard the Cloud-Aerosol Lidar and  
289 Infrared Pathfinder Satellite Observation (CALIPSO) satellite. The CALIPSO satellite  
290 was launched into a Sun-synchronous orbit on 28 April 2006. CALIOP is a dual-  
291 wavelength polarization lidar and is designed to acquire vertical profiles of attenuated  
292 backscatter from a near nadir-viewing geometry during both day and night phase (Winker  
293 et al., 2007; Liu et al., 2004, 2008; Hu et al., 2007, 2009). In this study, the aerosol  
294 extinction profiles at a nominal horizontal resolution of 5 km from the CALIPSO Level 2  
295 profile products are used to evaluate the model. We focus on the CALIOP nighttime  
296 observations in cloud-free condition, because nighttime observations have higher  
297 accuracy than daytime observations (Winker et al., 2009).

298 The cloud-aerosol discrimination (CAD) score, which is an indicator that  
299 measures confidence level of the discrimination between clouds (positive value) and  
300 aerosols (negative value), is used to help screen out aerosol profiles that contain cloud  
301 signals. We include the aerosol data with CAD score between -20 and -100, the same as  
302 Yu et al., (2010, 2015). The other screening is to exclude aerosol layers where the  
303 retrieval algorithm has to adjust the initially selected lidar ratio that is based on the type  
304 and subtype of the aerosol layer to be analyzed. It should be noted that when the aerosol

305 extinction is not detected by CALIOP, we set its value and also the corresponding model  
306 result equal to zero, and then we compare CALIOP extinction profiles with the model  
307 and analyze the seasonal variation.

## 308 **3.2 Ground-based observations**

### 309 **3.2.1 AERONET**

310 The AErosol RObotic NETwork (AERONET) is a globally distributed remote  
311 sensing network for aerosol monitoring from ground stations (Holben et al., 1998).  
312 AERONET uses the Cimel sun/sky photometer that measures AOD in 16 spectral  
313 channels (340-1640 nm). The measurements provide products every 15 minutes during  
314 daytime. In addition, an inversion algorithm is used for the retrieval of aerosol size  
315 distribution, complex refractive index, single-scattering albedo, and phase function  
316 (Dubovik and King, 2000; Dubovik et al., 2002). The spectral AOD from AERONET has  
317 an accuracy of  $\pm 0.01$  (Eck et al., 1999; Holben et al., 2001). In the analysis presented in  
318 this paper, the cloud screened and quality assured level 2.0 products are used. AERONET  
319 products do not measure at wavelength  $0.55 \mu\text{m}$ , so we calculate them through using the  
320 Angstrom exponent and the values at two nearest wavelengths  $0.5 \mu\text{m}$  and  $0.675 \mu\text{m}$ . The  
321 AERONET sites are located along the trans-Pacific transport pathways, so the products  
322 are important for evaluating the model results. Five sites over East Asia, one island site  
323 over the North Pacific, and four sites over the western U.S. are selected for comparison as  
324 shown in Figure 1.

### 325 **3.2.2 IMPROVE**

326 The Interagency Monitoring for Protected Visual Environments (IMPROVE)  
327 network was initiated in 1985 by U.S. federal agencies including EPA, National Park

328 Services, Department of Agriculture-Forest Service, and other land management agencies  
329 as a part of the EPA Regional Haze program (Malm et al., 1994). The network monitors  
330 the visibility conditions and changes in national parks and wilderness areas on a long-  
331 term basis. The detail sample collection and analytical methodology have been given by  
332 Hand et al., (2011), and the data can be downloaded from  
333 (<http://views.cira.colostate.edu/fed/DataWizard/Default.aspx>). There are 15 sites (Fig. 1)  
334 along the west coast selected to compare with the surface aerosols of the model. In this  
335 study, the mass concentrations of sulfate, nitrate, EC, OC, and dust in PM<sub>2.5</sub> (particulate  
336 matter with aerodynamic diameter less than 2.5 μm) are used to evaluate the model. The  
337 fine dust is calculated following the formula (Malm et al., 1994; Zhao et al., 2013a):

$$338 \quad \text{PM}_{2.5}\text{-Dust} = 2.2[\text{Al}] + 2.49[\text{Si}] + 1.63[\text{Ca}] + 2.42[\text{Fe}] + 1.94[\text{Ti}]$$

339 Where [Al], [Si], [Ca], [Fe], and [Ti] represent the mass concentration of aluminum,  
340 silicon, calcium, iron, and titanium, respectively.

341

## 342 **4 Results**

### 343 **4.1 Wind fields and precipitation**

344 Winds and precipitation are two crucial meteorological factors playing important  
345 roles in aerosol emission, transport, and removal. The seasonal mean wind fields at 850  
346 hPa averaged for the period 2010-2014 from the WRF-Chem simulation are compared  
347 with the Modern-Era Retrospective analysis for Research and Applications (MERRA)  
348 reanalysis data (Rienecker et al., 2011) (Fig. 2). Strong westerly winds occur over the  
349 North Pacific throughout the seasons with a peak (up to 12 m/s; 5.48 m/s on spatial  
350 average) in boreal winter (DJF) followed by boreal spring (MAM) (4.46 m/s on spatial

351 average). The winds are weakest in boreal fall (SON) (4.1 m/s on spatial average). In  
352 general, the model can well reproduce the spatial pattern of winds across the Pacific with  
353 wind speeds of 4.1-5.41 m/s averaged spatially for the four seasons, with a spatial  
354 correlation coefficient of 0.98 throughout the seasons. Figure 3 shows the spatial  
355 distribution of seasonal mean precipitation from the Global Precipitation Climatology  
356 Project (GPCP) observation (Huffman et al., 2001) averaged for the period 2010-2014  
357 and the difference in the WRF-Chem simulation. Over East Asia, precipitation reaches a  
358 maximum during the boreal summer (JJA) followed by MAM. In the North Pacific basin,  
359 the largest precipitation occurs in DJF along the storm tracks with the maximum  
360 westerlies. Over the U.S. west coast, precipitation peaks during DJF and reaches a  
361 minimum in JJA. The simulation reasonably reproduces the spatial and seasonal  
362 variations of precipitation with spatial correlation coefficients of 0.89, 0.81, 0.81, and  
363 0.84 for DJF, MAM, JJA, and SON, respectively. The simulation overestimates annual  
364 mean precipitation averaged over the North Pacific (3.1 mm day<sup>-1</sup> and 4.2 mm day<sup>-1</sup>,  
365 respectively, from GPCP and WRF-Chem). The overestimation (more than 50%) is  
366 particularly over the Inter-Tropical Convergence Zone (ITCZ) and the western tropical  
367 Pacific that are south to the 20°N and the major pathway of trans-Pacific transport. The  
368 excessive precipitation over the tropical Pacific may be due to biases from the convective  
369 parameterizations in producing tropical precipitation in WRF, such as overestimation of  
370 precipitation efficiency from the simple treatment of cloud microphysical processes in  
371 convective clouds, and biases in the prescribed temperature and humidity reference  
372 profiles (e.g., Fonseca et al., 2015; Hagos et al., 2016). Short sensitivity experiments we

373 performed show that the WRF simulated tropical precipitation is sensitive to the choice  
374 of convective parameterizations (not shown).

375

## 376 **4.2 Aerosol optical depth**

### 377 4.2.1 Spatial and temporal variation

378 Figure 4 shows the spatial distributions of seasonal mean AOD at 550 nm across  
379 the Pacific from Asia to North America averaged for 2010-2014 from the retrievals of  
380 MODIS and MISR onboard Terra and the corresponding WRF-Chem simulation. The  
381 WRF-Chem simulated AOD at 600 nm and 400 nm are used to derive the AOD at 550  
382 nm (using the Angström exponent). In order to reduce the sampling discrepancy between  
383 the two retrievals, the daily results from the two satellite retrievals and simulation are  
384 sampled and averaged at the same time and location. This way of averaging leads to the  
385 blank areas of missing values, which are relatively large in JJA. Satellite retrievals show  
386 consistent spatial pattern with the spatial correlation coefficients of 0.65-0.88 for the four  
387 seasons. The MODIS retrieval shows higher AOD over the semi-arid regions (e.g.,  
388 Northwest China and the southwestern U.S.) than the MISR retrieval; however the  
389 MODIS retrieved AOD magnitude over these regions is significantly overestimated  
390 because of its large uncertainties in the assumed surface reflectance in semi-arid regions  
391 (Remer et al., 2005; Levy et al., 2013). In comparison, the MISR observations in the  
392 western U.S. show better quality presumably because of the multi-angle capability that  
393 allows for a better characterization of surface reflectance. Both retrievals indicate that  
394 AOD is high over the Asian continent and gradually decreases across the Pacific. High  
395 AOD coincides with the sub-tropical jet (30°N-50°N, Fig. 2) over the Pacific and results

396 from wind-induced increase in sea-salt loading and the Asian pollutant outflow. Seasonal  
397 variation of aerosols across the Pacific is evident, with peak AOD over the western  
398 Pacific in MAM and minimum AOD in JJA and SON. This seasonal variation is  
399 generally consistent with previous studies (Yu et al., 2008, 2012), although our sampling  
400 method results in more missing data from satellite retrievals in JJA than other seasons.  
401 Previous studies found that trans-Pacific transport of air pollutants is most efficient in  
402 MAM due to active cyclonic activity and that pollutants are lifted to the free troposphere  
403 where they can be rapidly transported across the Pacific by strong westerlies (e.g., Forster  
404 et al., 2004; Liang et al., 2004; Heald et al., 2006; Yu et al., 2008).

405 The WRF-Chem simulation generally well captures the observed spatial and  
406 seasonal variability of AOD across the Pacific with the spatial correlation coefficients of  
407 0.63-0.76 for the four seasons against the MISR retrievals. The model generally  
408 underestimates the retrieved AOD over the North Pacific ( $0^{\circ}$ - $60^{\circ}$ N,  $120^{\circ}$ E- $120^{\circ}$ W) with  
409 an annual mean value of 0.11, which is lower than the retrieved values of 0.14 (MODIS)  
410 and 0.15 (MISR). Over the region north of  $20^{\circ}$ N ( $20^{\circ}$ N- $60^{\circ}$ N,  $120^{\circ}$ E- $120^{\circ}$ W), the  
411 simulation produces an average AOD of 0.14 that is more consistent with the retrieved  
412 values of 0.15 (MODIS) and 0.16 (MISR). This negative bias of the oceanic AOD south  
413 of  $20^{\circ}$ N may be due to underestimation of marine emissions (Yu et al., 2003) and/or  
414 overestimation of aerosol wet removal associated with the positive bias in precipitation  
415 (Fig. 3). The discrepancy may also be due to the higher uncertainty at low aerosol level  
416 (Levy et al., 2013) and cloud contamination in the retrievals that leads to an  
417 overestimation of AOD in some regions of the North Pacific (e.g., Zhang and Reid, 2006).  
418 The model also simulates lower AOD over the continent of North America compared

419 with satellite retrievals. The difference between the simulation and retrievals may be due  
420 to the uncertainty in satellite retrievals over the continents (e.g., Liu et al., 2004; Levy et  
421 al., 2010).

422 Since this study focuses on the trans-Pacific transport and evolution of aerosols,  
423 the Pacific is further divided into three sub-regions (Region 1: 20°N-50°N and 120°E-  
424 140°E; Region 2: 20°N-50°N and 140°E-140°W; Region 3: 20°N-50°N and 140°W-  
425 120°W) representing the West Pacific, the Central Pacific, and the East Pacific shown as  
426 the black boxes in Figure 4 for analysis. Figure 5 shows the seasonal mean 550 nm AOD  
427 over the three sub-regions from the MISR and MODIS retrievals and the corresponding  
428 WRF-Chem simulation at the pass time of MISR and MODIS, respectively, averaged for  
429 2010-2014. The retrievals show clearly that AOD peaks in MAM followed by DJF in all  
430 the regions across the Pacific. The simulated annual mean AOD of 0.21, 0.16, and 0.09  
431 over the West, Central, and East Pacific, respectively, successfully reproduce the  
432 observed values of 0.22, 0.16, and 0.10 from MODIS and 0.21, 0.16, and 0.10 from  
433 MISR. The simulation also captures the seasonal variability with the maximum AOD in  
434 MAM followed by DJF. In general, the MODIS and MISR retrievals and simulation  
435 consistently show that AOD reduces from the West Pacific to the East Pacific. The  
436 interannual variability of AOD over the three sub-regions is small for 2010-2014  
437 indicated by the retrievals and simulation (not shown).

438 Available observations from several AERONET sites (Fig. 1) over East Asia, the  
439 Pacific, and the western U.S. are also compared with the model simulation. Figure 6  
440 shows the comparison of observed and simulated AOD at three representative  
441 AERONET sites for 2010-2014 over East Asia, an island of the Pacific, and the western

442 U.S. coast. The observations and simulation agree well at all three sites, and both reflect  
443 the AOD gradient from East Asia to the western U.S. as shown in Figure 4. Observed  
444 AOD is the highest with a mean value of 0.31 at the SACOL site over East Asia and  
445 reduces to 0.075 at the Midway\_Island site, and 0.045 at the Frenchman\_Flat site. The  
446 model reproduces exactly these values at the three sites with correlation coefficients of  
447 0.45, 0.65, and 0.64, respectively. About 90% of simulated AOD is within a factor of 2 of  
448 the AERONET measurements.

449 Figure 7 further shows the monthly variation of AOD averaged at the AERONET  
450 sites over East Asia, the Pacific island, and the West U.S. (as shown in Fig. 1) from the  
451 AERONET observations, MODIS and MISR retrievals, and WRF-Chem simulation. For  
452 the simulated AOD, contributions by dust, BC, OC, sulfate, and other aerosols are also  
453 shown. Over East Asia, the MISR and AERONET retrievals agree well with the annual  
454 mean of 0.37 and 0.33, respectively. Their monthly variation correlates with a coefficient  
455 of 0.8. The MODIS retrievals with the annual mean of 0.48 generally overestimate AOD  
456 against the AERONET retrievals and correlate with the AEROENT retrieved monthly  
457 AOD with a coefficient of 0.67. The simulation reproduces the AERONET observed  
458 AOD variability with an annual mean of 0.38 and a monthly correlation coefficient of  
459 0.74. Model results show that anthropogenic aerosols dominate the AOD from summer to  
460 winter while dust can significantly contribute to the AOD in spring. Over the island of  
461 Pacific (the Midway\_Island site), retrievals from AERONET, MODIS, and MISR are  
462 generally consistent with each other on annual mean with values of 0.14, 0.13, and 0.14,  
463 respectively. The MISR retrievals correlate well with the AERONET retrievals in  
464 monthly variation with a coefficient of 0.70, which is 0.42 for MODIS, showing a

465 minimum in summer months. The simulated annual mean AOD of 0.14 well reproduces  
466 the AERONET retrieval. The model also captures the AERONET retrieved monthly  
467 variation of AOD with a correlation coefficient of 0.64. The simulation shows that this  
468 monthly variation is largely determined by the variation of sea-salt aerosol (e.g., Smirnov  
469 et al., 2003) and Asian pollutant outflow. The trans-Pacific transported aerosols (other  
470 than sea-salt) show strong monthly variation with a maximum in April and a minimum in  
471 July. Over the western U.S., the MISR and MODIS retrievals well capture the monthly  
472 variation of AERONET retrievals with correlation coefficients of  $\sim 0.9$ , but MISR and  
473 MODIS retrieve an annual mean AOD of 0.12 and 0.20, respectively, which are higher  
474 than the AERONET retrieval of 0.07, particularly in March-October. The simulated  
475 annual mean AOD of 0.07 reproduces the AERONET retrieval. The simulation also  
476 correlates well with the AERONET retrievals with a coefficient of 0.76 in monthly  
477 variation. Both the AERONET retrieval and simulation show that the largest AOD occurs  
478 in the spring months, which has significant contribution from the dust aerosol transported  
479 across the Pacific (to be discussed in Section 4.5). The simulation compares more  
480 consistently with the AERONET retrieval than with the MISR and MODIS retrievals in  
481 terms of magnitude, which suggests that the difference between the MODIS and MISR  
482 retrievals and the simulation over the western U.S. shown in Figure 4 is largely due to  
483 uncertainties associated with the satellite retrievals. The simulation underestimates the  
484 AERONET retrieved AOD in July-September. This underestimation may come from the  
485 model significant negative biases in carbonaceous aerosols in the warm season (to be  
486 discussed in Section 4.5).

487

#### 488 4.2.2 Wavelength dependence

489           The wavelength dependence of AOD that can be represented by the extinction  
490 Angstrom exponent (EAE) is an indicator of aerosol particle size (Angstrom, 1929;  
491 Schuster et al., 2006). In general, relatively small values of EAE indicate that aerosol size  
492 distributions are dominated by coarse aerosols typically associated with dust and sea-salt,  
493 while relatively large values of EAE indicate fine aerosols usually contributed by  
494 anthropogenic pollution and biomass burning. Figure 8 shows the seasonal mean EAE  
495 averaged for 2010-2014 from the MODIS retrievals and the WRF-Chem simulation over  
496 the three sub-regions. The retrievals show clearly that the seasonal median EAE values  
497 peak at 1.25, 0.74, and 0.89 in JJA and reach a minimum of 0.68, 0.20, and 0.21 in DJF  
498 in three sub-regions of the West, Central, and East Pacific, respectively. This seasonality  
499 reflects the fact that photochemistry is most active in JJA to produce fine aerosol particles  
500 such as sulfate. In general, the simulation successfully reproduces the observed EAE  
501 seasonality with the JJA maximum of 1.09, 0.82, and 0.79 and the DJF minimum of 0.83,  
502 0.42, and 0.35 in the three sub-regions, respectively. The retrievals and simulation also  
503 show that the values of EAE are greater in the West Pacific than in the Central and East  
504 Pacific. This pattern may reflect the dominance of the Asian pollutant outflow on the  
505 aerosol size distributions over the West Pacific, while the relatively large-size particles of  
506 sea-salt dominates in the other two regions. Again, the annual variability of EAE over the  
507 three sub-regions is small (not shown).

508

#### 509 **4.3 Aerosol absorption optical depth**

510 Light absorbing aerosols such as BC and dust play an important role in the  
511 atmosphere to absorb radiation and change the heating profiles in the atmosphere.  
512 Aerosol absorption optical depth (AAOD) is an important parameter for evaluating the  
513 model performance in simulating light absorbing aerosols. Figure 9 shows the seasonal  
514 mean AAOD at 500 nm averaged for 2010-2014 and over the three sub-regions from the  
515 OMI retrieval and the WRF-Chem simulation. The model simulated AAOD at 600 nm  
516 and 400 nm are used to derive the AAOD at 500 nm (using the Angström exponent).  
517 Both retrievals and simulation show small interannual variability (not shown). The  
518 simulated seasonal mean AAOD of 0.015 over the West Pacific agrees reasonably well  
519 with the OMI retrieval of 0.014 in DJF but is higher in the other three seasons, with the  
520 largest difference in JJA. The significantly lower AAOD in seasons other than DJF from  
521 the OMI retrieval is also shown in the comparison with the AERONET retrieval (to be  
522 discussed with Fig. 10). Over the Central Pacific, the simulated seasonal mean AAOD of  
523 0.014 and 0.006 in MAM and SON, respectively, generally reproduces the retrieved  
524 AAOD of 0.017 and 0.005, but the model overestimates (underestimates) the retrieved  
525 values in JJA (DJF) with 0.008 (0.005) from the simulation and 0.004 (0.009) from the  
526 retrieval. This difference may reflect the model deficiency in simulating Asian BC  
527 outflow over the Pacific in JJA and DJF, but may also result from retrieval uncertainties.  
528 The OMI retrievals may have difficulty in distinguishing the ocean color effects from  
529 those of low aerosol concentrations in the UV spectral range and ignoring the less-  
530 sufficient amounts of absorbing aerosols (Veihelmann et al., 2007; Torres et al., 2013).  
531 Jethva et al. (2014) found that the most important source of uncertainty in OMI AAOD is  
532 the effect of sub-pixel cloud contamination related to the sensor's coarse spatial

533 resolution, which causes AAOD underestimations for cases of low aerosol load. Over the  
534 East Pacific, the simulated seasonal mean AAOD of 0.0035, 0.0091, 0.0048, and 0.0042  
535 for DJF, MAM, JJA, and SON, respectively, are generally consistent with the retrieved  
536 values of 0.005, 0.007, 0.0012, and 0.003, which shows the maximum value in MAM.  
537 The most significant difference occurs in JJA. Similar as over the Central Pacific, the  
538 underestimation of retrieved AAOD over the clean region may contribute to the  
539 difference. The retrievals and simulation show large variability of AAOD, and they  
540 generally agree within the 10th and 90th percentiles of each other. AAOD is larger over  
541 the West Pacific than the Central and East Pacific, which is consistent with the AOD  
542 pattern. The simulation shows that AAOD peaks in MAM followed by JJA over the three  
543 sub-regions, which may be due to the stronger outflow of dust and anthropogenic  
544 pollutants in the two seasons.

545         The AERONET retrieval products (version 2) also provide AAOD values but  
546 only at the sites and time when the total AOD exceeds a threshold value of 0.4 at 440 nm  
547 because the AERONET inversion algorithms require a high signal-to-noise ratio to  
548 retrieve some optical products such as AAOD. The total AOD values over the Central  
549 Pacific and the western U.S. are less than this threshold value most of the time, and only  
550 AAOD values retrieved at the East Asian sites are available and reliable. Figure 10 shows  
551 the monthly variation of AAOD averaged at the AERONET sites over East Asia (Fig. 1)  
552 from the AERONET observation, OMI retrieval, and WRF-Chem simulation. The  
553 AERONET retrieval shows the monthly variation of AAOD over East Asia with  
554 relatively lower values in JJA probably due to wet removal of aerosols by precipitation  
555 and mixing with clean marine air during the East Asian summer monsoon (Zhao et al.,

556 2010). The simulation generally captures the observed monthly variability with the  
557 minimum AAOD of 0.035 and 0.032 in July from the simulation and the AERONET  
558 retrieval, respectively, and the maximum of 0.055 and 0.054 in October, respectively.  
559 The model overestimates AAOD in the warm months (May-September) with the mean  
560 values of 0.046 and 0.036 from the simulation and retrieval, respectively, and  
561 underestimates AAOD in December and January with the mean values of 0.037 and  
562 0.043, respectively. The model positive (negative) biases in AAOD in the warm (cold)  
563 months may be partly related to the constant anthropogenic BC emissions applied  
564 throughout the seasons, but previous studies have shown that anthropogenic BC  
565 emissions over China may have seasonal variation, with roughly 6% versus 13% of the  
566 annual total BC emission in summer and winter, respectively, estimated in Lu et al.  
567 (2011). The simulation shows that AAOD over East Asia is dominated by BC and is  
568 partly contributed by dust. Other aerosols contribute to small amount of AAOD due to  
569 the internal mixing of aerosols in the atmosphere (Zhao et al., 2013a). The OMI retrieved  
570 AAOD is lower than that from AERONET and WRF-Chem, particularly in JJA and SON.  
571 The lower OMI AAOD over East Asia may also indicate its negative biases over the  
572 West Pacific (Fig. 9) where the air is significantly affected by the East Asian outflow.  
573 The biases in the OMI algorithm of retrieving SSA over East Asia may be also applied  
574 over the West Pacific.

575

#### 576 **4.4 Aerosol vertical distributions**

577 Column integrated properties of aerosol (e.g., AOD and AAOD) provide useful  
578 information in regard to atmospheric aerosol loading but little information on the vertical

579 distribution of aerosols. Previous studies have found that simulated aerosol vertical  
580 distributions differ significantly, which can affect the assessments of aerosol impacts on  
581 climate and air quality (e.g., Schulz et al., 2006; Textor et al., 2006). CALIPSO with the  
582 unique capability provides an opportunity to assess model simulation of aerosol vertical  
583 distributions (e.g., Huang et al., 2013). Figure 11 shows the vertical distributions of  
584 annual mean aerosol extinction coefficients for 2010-2014 averaged over the three sub-  
585 regions from the CALIPSO retrieval and the corresponding WRF-Chem simulation under  
586 cloud-free condition. The model results are sampled for averaging at the locations and  
587 times where and when retrievals are available. The CALIPSO retrieval shows clearly that  
588 aerosol extinction coefficients peak near several hundred meters above the surface and  
589 then decrease with the altitude over the three sub-regions. The extinction coefficients  
590 reduce from the West to East Pacific. The model generally reproduces the aerosol  
591 extinction vertical variation with correlation coefficients of 0.95-0.97. The simulated  
592 aerosol extinction coefficients are consistent with the retrievals around 0.5-1 km with  
593 difference within 15%. The difference increases in the free troposphere and below 0.5 km.  
594 The simulation is higher than the retrieval in the free troposphere (e.g., about a factor of 2  
595 around 4 km), which may be due to the reduced sensitivity of CALIPSO to tenuous  
596 aerosol layers above 4 km (Yu et al., 2010). The lower (up to 30% lower) simulated  
597 extinction coefficients below 0.5 km in all three sub-regions may indicate negative biases  
598 in estimating marine aerosol emissions and excessive wet scavenging of the model, as  
599 shown in Fig. 4. The in-situ measurements over the region are needed for further  
600 validating both remote sensing data and the simulation. The simulated mass fraction of  
601 each aerosol component (Fig. 12) shows that below 1 km, sea-salt dominates the total

602 aerosol mass over the Central and East Pacific, while the outflow of anthropogenic  
603 aerosols and dust also makes significant contributions over the West Pacific. Above 4 km,  
604 dust is the dominant aerosol over all three sub-regions.

605         The seasonal variation of aerosol extinction profiles averaged for 2010-2014 (Fig.  
606 13) shows the spring maximum, particularly above 2 km, over all three sub-regions from  
607 both the CALIPSO retrievals and the model simulation. This is likely due to the  
608 seasonality of dust outflow over the Pacific (Fig. 14) that dominates the aerosol masses  
609 above 2 km with a peak in spring (e.g., Huang et al. 2013). The model reasonably  
610 reproduces the retrieved aerosol extinction vertical variation through the seasons over the  
611 three sub-regions with the correlation coefficients of 0.93-0.98. Over the West Pacific,  
612 the simulation has larger negative biases (up to 35%) below 1 km in DJF when sea-salt  
613 has a relatively larger contribution near the surface (Fig. 14) than other seasons (up to 15-  
614 25%), and has positive biases above 1 km. At 1-4 km, the simulated aerosol extinction is  
615 higher (up to a factor of 2) than the retrieval and the difference increases with the altitude.  
616 The comparison between the simulation and retrieval at 1-4 km is the best in DJF with  
617 the difference within 15%. In JJA, the aerosol mass has the largest contribution from the  
618 anthropogenic pollutant outflow among the seasons with a peak at ~ 2 km above the  
619 surface. Over the Central and East Pacific, the model has smaller negative biases (up to  
620 20%) below 1 km than over the West Pacific and the maximum negative bias is in DJF.  
621 Over these two regions, the seasonality of the vertical shape of each aerosol component  
622 contribution is similar to that over the West Pacific, except that the sea-salt contribution  
623 is larger near the surface (Fig. 14).

624

#### 625 **4.5 Aerosol surface mass concentrations over the West U.S.**

626 For lack of in-situ observations of aerosol masses over the Pacific, measurements  
627 of surface fine aerosol ( $PM_{2.5}$ ) component mass concentrations from the IMPROVE  
628 network over the western U.S. were widely used for model evaluation of trans-Pacific  
629 transport (e.g., Chin et al., 2007; Hadley et al., 2007). Daily variation of surface fine  
630 aerosols (dust, sulfate, nitrate, BC, and OC) averaged for 2010-2014 from the IMPROVE  
631 measurements and the monthly mean of measurements and corresponding model  
632 simulation are illustrated in Figure 15. The IMPROVE sites over the western U.S. (Fig. 1)  
633 that have measurements for the entire five years (2010-2014) and with less noisy values  
634 are divided at  $40^\circ N$  into two groups to represent the Northwest and Southwest U.S. The  
635 averaged values over the Northwest and Southwest sites are shown.

636 At both Northwest and Southwest sites, the model generally captures the observed  
637 monthly variation of dust with the correlation coefficients of 0.61 and 0.55, respectively.  
638 Both the observation and simulation show the maximum dust mass concentration in  
639 MAM and the minimum in DJF. The model simulates higher annual mean surface dust  
640 concentrations ( $0.25 \mu g m^{-3}$  and  $0.56 \mu g m^{-3}$  over the Northwest and Southwest,  
641 respectively) than the observation ( $0.18 \mu g m^{-3}$  and  $0.35 \mu g m^{-3}$ , respectively). The  
642 observed surface sulfate concentrations are the lowest in the cold season ( $0.17 \mu g m^{-3}$  and  
643  $0.18 \mu g m^{-3}$  in DJF over the Northwest and Southwest, respectively) when  
644 photochemistry is least active, and the highest in the warm season ( $0.47 \mu g m^{-3}$  and  $0.63$   
645  $\mu g m^{-3}$  in June-September, respectively) when the most active photochemistry occurs.  
646 This seasonality of sulfate may also be contributed by the seasonality of wet removal  
647 (much more precipitation in DJF). Over the Northwest and Southwest, the simulation

648 generally reproduces the magnitude and seasonality of sulfate with the minimum surface  
649 concentrations of  $0.17 \mu\text{g m}^{-3}$  and  $0.25 \mu\text{g m}^{-3}$ , respectively, in DJF and the maximum  
650 surface concentrations of  $0.49 \mu\text{g m}^{-3}$  and  $0.62 \mu\text{g m}^{-3}$ , respectively, in June-September,  
651 and monthly correlation coefficients of 0.78 and 0.83, respectively. Nitrate shows a  
652 seasonality that is opposite to that of sulfate, with a maximum surface concentration  
653 occurring in the cold season ( $0.72 \mu\text{g m}^{-3}$  and  $1.22 \mu\text{g m}^{-3}$  in DJ over the Northwest and  
654 Southwest, respectively) and a minimum in the warm season ( $0.25 \mu\text{g m}^{-3}$  and  $0.35 \mu\text{g m}^{-3}$   
655 in JJA, respectively), which can be explained by the combined effects of temperature  
656 and vertical turbulent mixing (Zhao et al., 2013a). The simulation generally reproduces  
657 the seasonality of nitrate with a monthly correlation coefficient of 0.75 and 0.83 over the  
658 Northwest and Southwest, respectively. Over the Northwest and Southwest, the model  
659 simulates reasonably the maximum surface nitrate concentration of  $0.69 \mu\text{g m}^{-3}$  and  $1.35$   
660  $\mu\text{g m}^{-3}$ , respectively, in the cold season and the minimum with values of  $0.18 \mu\text{g m}^{-3}$  and  
661  $0.42 \mu\text{g m}^{-3}$ , respectively, in the warm season. The simulation has relatively larger  
662 positive biases (a factor of 2) in months (February, March, October, and November)  
663 between the cold and warm seasons, which may reflect the model deficiency in aerosol  
664 thermodynamics (i.e., the partitioning of nitrate aerosol to the gas phase in these months  
665 is too slow in the model). In general, both observation and simulation show higher  
666 surface dust, sulfate, and nitrate concentrations over the Southwest than the Northwest.

667 A sensitivity simulation without dust, fire, and anthropogenic emissions over  
668 North America ( $10^{\circ}\text{N}$ - $70^{\circ}\text{N}$  and  $170^{\circ}\text{W}$ - $60^{\circ}\text{W}$ ) indicates that the trans-Pacific  
669 transported dust dominates the total dust amount in all seasons at the northern and  
670 southern sites with the contribution of 80% and 60%, respectively, on annual mean,

671 particularly in MAM with the contribution of >90% and ~85%, respectively. At the  
672 southern sites, the trans-Pacific dust makes the lowest contribution of 19% in DJF. The  
673 large contribution of trans-Pacific dust indicates that the simulated overestimation of  
674 surface dust concentrations may be resulted from the excessive trans-Pacific transport of  
675 dust, which is also indicated in the comparison with the CALIPSO retrieval that shows  
676 the simulated aerosol extinction is overestimated above 1 km over the North Pacific. The  
677 difference may also be partly from the observation uncertainties. As described in Section  
678 3.2.2, the mass of soil dust is calculated from a linear combination of the measured  
679 elements associated predominantly with soil, including Al, Si, Ca, Fe, and Ti. The  
680 uncertainties associated with the reported dust values reflect the range and variation of  
681 mineral composition from a variety of soil types. The sensitivity simulation also shows  
682 that trans-Pacific transported sulfate can make significant contribution to its surface  
683 concentration over the western U.S., and the relative contributions are larger when the  
684 surface concentrations are lower with ~60% in DJF averaged at all sites and ~35% in JJA.  
685 The trans-Pacific nitrate contributes a relatively small amount (~15%) to the total nitrate  
686 surface concentration.

687       There is a significant difference in BC and OC surface concentrations between the  
688 observations and simulation. At the Northwest sites, the observed BC and OC show  
689 significant seasonal variation with the highest surface concentration in June-September  
690 (JJAS). The sensitivity simulation shows that the peak is dominated by the North  
691 American emission that is contributed by biomass burning with a maximum in JJAS  
692 (Chin et al., 2007). The simulation captures this seasonality to some extent with monthly  
693 correlation coefficients of 0.74 and 0.69 for BC and OC, respectively. However, the

694 simulation significantly underestimates the JJAS peak with  $0.05 \mu\text{g m}^{-3}$  and  $0.49 \mu\text{g m}^{-3}$   
695 BC and  $0.5 \mu\text{g m}^{-3}$  and  $4.5 \mu\text{g m}^{-3}$  OC from the simulation and observation, respectively.  
696 These significant negative biases in the model are likely from uncertainties in the  
697 GFEDv3 biomass burning inventory for the simulation period. The monthly mean  
698 emissions at a relatively coarse horizontal resolution may not be able to capture the  
699 strong local fire events. Mao et al. (2011) pointed out that the GFED inventory may  
700 underestimate the magnitude of biomass burning emissions in the western U.S. due to the  
701 issue of detecting small fires, for example, from prescribed and agricultural burning (e.g.,  
702 Randerson et al., 2012; Giglio et al., 2010). Mao et al. (2014) estimated that the biomass  
703 burning BC emissions inverted from the IMPROVE observations can be a factor of 5  
704 higher than the GFED inventory in July-September over the Western U.S. Another  
705 biomass burning emission inventory FINN (Fire INventory from Near) (Wiedinmyer et  
706 al., 2011) also shows a factor of 3 higher BC emissions than the GFED inventory over the  
707 Northwest U.S. ( $100^{\circ}\text{W}$ - $125^{\circ}\text{W}$  and  $40^{\circ}\text{N}$ - $50^{\circ}\text{N}$ ) in September 2011 (not shown).

708 At the Southwest sites, the impact of biomass burning on the BC and OC surface  
709 concentrations seems relatively small. The observations show the maximum BC surface  
710 concentration of  $0.17 \mu\text{g m}^{-3}$  in DJF and the minimum of  $0.09 \mu\text{g m}^{-3}$  in JJA, which is  
711 likely due to stronger vertical turbulent mixing in JJA compared with DJF (Zhao et al.,  
712 2013a). The simulation can well capture the magnitude and seasonality of surface BC  
713 concentration with the monthly correlation coefficient of 0.78 and the maximum of  $0.19$   
714  $\mu\text{g m}^{-3}$  in DJF and the minimum of  $0.10 \mu\text{g m}^{-3}$  in JJA. The observed OC still shows the  
715 peak concentration of  $1.27 \mu\text{g m}^{-3}$  in JJA, and the model significantly underestimates the  
716 peak OC concentration with a value of  $0.20 \mu\text{g m}^{-3}$ . The negative bias of OC over the

717 Southwest seems not to be related to the underestimation of biomass burning because BC  
718 is reasonably simulated. This seasonal variability may be determined by the secondary  
719 production of OC, which peaks in JJA because photochemistry is more active and  
720 emissions of biogenic volatile organic compounds are higher in the warm season. The  
721 underestimation of secondary organic aerosol (SOA) may be due to the uncertainty of  
722 biogenic emissions (Zhao et al., 2016) and the outdated SOA mechanism used in the  
723 current version of WRF-Chem (Shrivastava et al., 2011). Besides the emission and model  
724 deficiency, another source of the difference between the simulation and observation may  
725 be from the sub-grid variability of emissions and surface concentrations that confounds  
726 the comparison of model simulation at one-degree horizontal grid resolution and the point  
727 measurements from the individual sites. On the other hand, it is also noteworthy that  
728 uncertainties in the IMPROVE carbonaceous aerosol data are also relatively high because  
729 they are inferred from optical/thermal measurements. The sensitivity simulation again  
730 shows that the peaks of BC and OC surface concentrations are dominated by the North  
731 American emissions.

732

## 733 **5 Summary and conclusion**

734 A fully coupled meteorology-chemistry model (WRF-Chem) has been configured  
735 to conduct quasi-global simulation for the 5 years of 2010-2014. The simulation results  
736 are evaluated for the first time with various reanalysis and observational datasets,  
737 including precipitation from GPCP, wind fields from MERRA, AOD, EAE, and AAOD  
738 from MODIS, MISR, OMI, and AERONET, aerosol extinction profiles from CALIPSO,  
739 and aerosol surface mass concentrations from IMPROVE. In this study, the evaluation

740 and analysis focus on the trans-Pacific transport region for the purpose of demonstrating  
741 the capability of using the quasi-global WRF-Chem simulation to provide consistent  
742 lateral chemical boundaries for nested regional WRF-Chem simulations that can be used  
743 to investigate the impact of trans-Pacific transported aerosols on the regional air quality  
744 and climate over the western U.S. The main conclusion is summarized below:

745 ■ The comparison of simulated AOD with the satellite and AERONET retrievals  
746 reveals that the model can well capture the spatial gradient of aerosol mass loading  
747 decreasing from the West to East Pacific, resulting from the sea-salt loading and the  
748 Asian pollutant outflow. The seasonal variation of aerosols across the Pacific with the  
749 maximum AOD in MAM is also reproduced by the model. The model underestimates  
750 AOD over the ocean to the south of 20°N and over the continent of North America  
751 against the satellite retrievals. This discrepancy may reflect the model  
752 underestimation of marine emissions and/or overestimation of aerosol wet removal or  
753 the positive retrieval errors due to cloud-contamination. Compared with the  
754 AERONET retrieval, the difference of AOD over the western U.S. between the  
755 simulation and satellite retrievals may be due to the uncertainty in the satellite  
756 retrievals over the continent.

757 ■ The assessment of simulated EAE indicates that the model generally captures the  
758 observed smaller-size aerosols over the West Pacific contributed by the Asian  
759 pollutant outflow compared to the relatively larger particles over the Central and East  
760 Pacific with more contributions from sea-salt. The model also simulates the consistent  
761 seasonality of EAE with observations showing a minimum in DJF and a maximum in  
762 JJA due to the active production of small particles in warm seasons.

- 763   ▪ The model reasonably simulates the decreasing gradient of OMI derived AAOD from  
764   the East to West of Pacific. The simulation shows a peak of AAOD in MAM due to  
765   the strong outflow of dust and anthropogenic pollutants. The comparison with  
766   AERONET retrieved AAOD over East Asia may indicate that the OMI SSA retrieval  
767   has positive biases over East Asia and also the West Pacific, particularly in JJA. Over  
768   East Asia, the model positive (negative) biases in AAOD in the warm (cold) months  
769   may be partly due to the neglect of the seasonal variability of anthropogenic BC  
770   emissions in this study.
- 771   ▪ The model generally captures the CALIPSO retrieved vertical gradient of aerosol  
772   extinction coefficients roughly decreasing with the altitude over the Pacific. Near the  
773   surface, the model biases in estimating marine aerosol emissions may contribute to  
774   the discrepancy between the simulation and retrievals. The difference between the  
775   simulation and retrievals in the free troposphere may be due to the reduced sensitivity  
776   of CALIPSO to the aerosol layers above 4 km. The model well captures the  
777   seasonality of aerosol extinction profiles with a maximum in MAM, which is largely  
778   controlled by the activity of dust outflow events over the Pacific.
- 779   ▪ Compared with the measurements from the IMPROVE sites over the western U.S.,  
780   the model simulates reasonable magnitudes and seasonality of the observed sulfate  
781   and nitrate surface concentrations with peaks in JJA and DJF, respectively. The  
782   simulation has relatively larger positive biases of nitrate surface concentrations in  
783   early spring and late fall, which may reflect the model deficiency in aerosol  
784   thermodynamics that the partitioning of nitrate aerosol to the gas phase in these  
785   months is too slow in the model. The simulation captures the observed seasonality of

786 dust surface concentrations with the maximum and minimum in MAM and DJF,  
787 respectively, but generally overestimates the observed dust surface concentrations,  
788 which may be due to the excessive trans-Pacific dust. The difference may also be  
789 partly from the observation uncertainties. Over the southwestern U.S., the simulation  
790 reproduces the magnitude and seasonality of surface BC concentrations that show the  
791 maximum in DJF, but significant underestimates the surface OC concentrations in  
792 JJA likely due to the negative biases in SOA production. Over the northwestern U.S.,  
793 the simulation significantly underestimates surface BC and OC concentrations likely  
794 due to the uncertainties in fire emissions that may not capture the strong local fire  
795 events. Another source of the difference may be due to the discrepancy in spatial  
796 scales between site observations and model outputs for the grid cell area of one-  
797 degree resolution. In addition, uncertainties in IMPROVE may also contribute to the  
798 discrepancy, in particular for carbonaceous aerosols that are inferred from  
799 optical/thermal measurements.

800 ■ The sensitivity simulation shows that the trans-Pacific transported dust dominates the  
801 dust surface concentrations in the western U.S., particularly in MAM. The trans-  
802 Pacific transported sulfate and nitrate can also make significant contribution to their  
803 surface concentrations over the rural areas of the western U.S. The peaks of BC and  
804 OC surface concentrations over the western U.S. are dominated by the North  
805 American emissions. These sensitivity simulation results may be different to some  
806 extent from other models (e.g., Chin et al., 2007), which could result from the  
807 considerable differences in aerosol composition and vertical distributions due to  
808 differences in model treatments of emissions and removal processes as revealed by

809 several inter-comparison studies (Barrie et al., 2001; Penner et al., 2002; Textor et al.,  
810 2006). More detailed model inter-comparison of the trans-Pacific transport of  
811 aerosols deserves further study.

812 Although dust and biomass burning emissions in general have considerable year-  
813 to-year variations, the interannual variability of seasonal AOD for 2010-2014 averaged  
814 over the three sub-regions of the Pacific is small as indicated by the retrievals and  
815 simulation. It is noteworthy that the trans-Pacific aerosols identified in this study include  
816 not only the outflow of Asian pollutants and dust but also European pollutants and  
817 African dust that are transported to Asia and then merged with the Asian outflow. This  
818 has been recognized by previous studies (e.g., Chin et al., 2007). The evaluation in this  
819 study successfully demonstrates that the WRF-Chem quasi-global simulation with some  
820 improvements in emission inventories can be used for studying trans-Pacific transport of  
821 aerosols and providing reasonable inflow chemical boundaries for the western U.S. to  
822 further understand the impact of transported pollutants on the air quality and regional  
823 climate with high resolution nested regional modeling. It needs to be noted that the  
824 aerosol optical properties, such as AOD, AAOD, and EAE, derived from the retrievals  
825 and simulation have some different assumptions of the physical and optical parameters,  
826 so that the link between the model and the satellite data are only qualitative or semi-  
827 quantitative. Evaluation of model results with in-situ observations would be informative.  
828 In-situ data even for specific events are valuable especially over Asia and the Pacific  
829 where public data are currently sparse or inaccessible, although some observations may  
830 be obtained through collaborations. Last but not least, the model biases against  
831 observations may be also partly contributed by the uncertainties in emissions. Some

832 recently updated anthropogenic emissions (e.g., Janssens-Maenhout et al., 2015; Li et al.,  
833 2016) and other biomass burning emissions with higher temporal and spatial resolutions  
834 (e.g., Wiedinmyer et al., 2011) may be used in future studies to investigate the impact of  
835 emission uncertainties on trans-Pacific aerosols over the West U.S.

836

### 837 **Code availability**

838 The WRF-Chem version 3.5.1 release can be obtained at  
839 [http://www2.mmm.ucar.edu/wrf/users/download/get\\_source.html](http://www2.mmm.ucar.edu/wrf/users/download/get_source.html). A general WRF-Chem  
840 user's guide is also available online (<http://ruc.noaa.gov/wrf/WG11/>). Code modifications  
841 include changes to the chemical boundary treatment using periodic boundary conditions  
842 in the zonal direction for quasi-global WRF-Chem simulation. Other changes to the  
843 model include the oceanic (sea salt and dimethyl sulfide) emission schemes and the  
844 convective transport and removal scheme of tracers that play a significant role in quasi-  
845 global WRF-Chem simulations of aerosols. These modifications and model configuration  
846 for conducting quasi-global WRF-Chem simulations here are available upon request by  
847 contacting the corresponding author and will be incorporated in the future available  
848 release of WRF-Chem.

849

### 850 **Acknowledgements**

851 This research was supported by the Office of Science of the U.S. Department of Energy  
852 (DOE) as part of the Regional & Global Climate Modeling (RGCM) program. J. Huang  
853 acknowledges support from the National Basic Research Program of China  
854 (2012CB955301). H. Yu was supported by NASA CALIPSO project (NNX14AB21G)

855 managed by Dr. David Considine. This study used computing resources from the PNNL  
856 Institutional Computing. Pacific Northwest National Laboratory is operated by Battelle  
857 Memorial Institute for the DOE under contract DE-AC05-76RL01830. The CALIPSO  
858 data were obtained from the NASA Langley Research Center Atmospheric Sciences Data  
859 Center. MODIS and MISR data were obtained from the NASA Atmospheric Science  
860 Data Center. OMI data were obtained from the NASA Goddard Earth Sciences Data and  
861 Information Services Center.

862

863

864 **Reference**

- 865 Ahn, C., O. Torres, and P. K. Bhartia: Comparison of Ozone Monitoring Instrument UV  
866 Aerosol Products with Aqua/Moderate Resolution Imaging Spectroradiometer and  
867 Multiangle Imaging Spectroradiometer observations in 2006, 113, D16S27,  
868 doi:10.1029/2007JD008832, 2008.
- 869 Alizadeh-Choobari, O., P. Zawar-Reza, and A. Sturman: The global distribution of  
870 mineral dust and its impacts on the climate system: A review, *Atmospheric Research*  
871 138, 152–165, doi:10.1016/j.atmosres.2013.11.007, 2014.
- 872 Alizadeh-Choobari, O., A. P. Sturman, and P. Zawar-Reza: Global distribution of mineral  
873 dust and its impact on radiative fluxes as simulated by WRF-Chem, *Meteorology and*  
874 *Atmospheric Physics*, 127(6), DOI: 10.1007/s00703-015-0390-4, 2015.
- 875 Anderson, T. L., Y. Wu, D. A. Chu, B. Schmid, J. Redemann, and O. Dubovik: Testing  
876 the MODIS satellite retrieval of aerosol fine-mode fraction, *J. Geophys. Res.*, 110,  
877 D18204, doi:10.1029/2005JD005978, 2005.
- 878 Angstrom, A. : On the atmospheric transmission of Sun radiation and on dust in the air,  
879 *Geogr. Ann*, 11, 156-166, 1929.
- 880 Ault, A. P., C. R. Williams, A. B. White, P. J. Neiman, J. M. Creamean, C. J. Gaston, F.  
881 M. Ralph, and K. A. Prather: Detection of Asian dust in California orographic  
882 precipitation, *J. Geophys. Res.*, 116, D16205, doi:10.1029/2010JD015351, 2011.
- 883 Barnard, J. C., J. D. Fast, G. Paredes-Miranda, W. P. Arnott, and A. Laskin: Technical  
884 Note: Evaluation of the WRF-Chem “Aerosol Chemical to Aerosol Optical  
885 Properties” Module using data from the MILAGRO campaign, *Atmos. Chem. Phys.*,  
886 10, 7325-7340, doi:10.5194/acp-10-7325-2010, 2010.

887 Barrie, L. A., Y. Yi, W. R. Leitch, U. Lohmann, P. Kasibhatla, G. J. Roelofs, J. Wilson,  
888 F. McGovern, C. Benkovitz, M. A. Melieres, K. Law, J. Prospero, M. Kritz, D.  
889 Bergmann, C. Bridgeman, M. Chin, J. Christensen, R. Easter, J. Feichter, C. Land, A.  
890 Jeuken, E. Kjellstrom, D. Koch, and P. Rasch: A comparison of large-scale  
891 atmospheric sulphate aerosol models (COSAM): overview and highlights, *Tellus*,  
892 53B, 615-645, 2001.

893 Binkowski, F. S., and Shankar, U.: The Regional Particulate Matter Model 1. Model  
894 description and preliminary results, *J. Geophys. Res.*, 100(D12), 26191-26209, 1995.

895 Chapman, E. G., Gustafson Jr., W. I., Easter, R. C., Barnard, J. C., Ghan, S. J., Pekour,  
896 M. S., and Fast, J. D.: Coupling aerosol-cloud-radiative processes in the WRF-Chem  
897 model: Investigating the radiative impact of elevated point sources, *Atmos. Chem.*  
898 *Phys.*, 9, 945–964, doi:10.5194/acp-9-945-2009, 2009.

899 Chen, S., J. Huang, C. Zhao, Y. Qian, L. R. Leung, and B. Yang: Modeling the transport  
900 and radiative forcing of Taklimakan dust over the Tibetan Plateau: A case study in the  
901 summer of 2006, *J. Geophys. Res.*, 118(2), 797-812, doi:10.1002/jgrd.50122, 2013.

902 Chen, S., C. Zhao, Y. Qian, L. R. Leung, J. Huang, Z. Huang, J. Bi, W. Zhang, J. Shi, L.  
903 Yang, D. Li, J. Li: Regional modeling of dust mass balance and radiative forcing over  
904 East Asia using WRF-Chem, *Aeolian Research*, 15, 15-30,  
905 doi:10.1016/j.aeolia.2014.02.001, 2014.

906 Chin, M., A. Chu, R. Levy, L. Remer, Y. Kaufman, B. Holben, T. Eck, P. Ginoux, and Q.  
907 Gao: Aerosol distribution in the Northern Hemisphere during ACE-Asia: Results  
908 from global model, satellite observations, and Sun photometer measurements, *J.*  
909 *Geophys. Res.*, 109, D23S90, doi:10.1029/2004JD004829, 2004.

910 Chin, M., T. Diehl, P. Ginoux, and W. Malm: Intercontinental transport of pollution and  
911 dust aerosols: implications for regional air quality, *Atmos. Chem. Phys.*, 7, 5501–  
912 5517, 2007.

913 Creamean, J. M., K. J. Suski, D. Rosenfeld, A. Cazorla, P. J. DeMott, R. C. Sullivan, A.  
914 B. White, F. M. Ralph, P. Minnis, J. M. Comstock, J. M. Tomlinson, and K. A.  
915 Prather: Dust and Biological Aerosols from the Sahara and Asia Influence  
916 Precipitation in the Western U.S., *Science*, 339, 1572, DOI:  
917 10.1126/science.1227279, 2013.

918 Dentener, F., S. Kinne, T. Bond, O. Boucher, J. Cofala, S. Generoso, P. Ginoux, S. Gong,  
919 J. J. Hoelzemann, A. Ito, L. Marelli, J. E. Penner, J. P. Putaud, C. Textor, M. Schulz,  
920 G. R. van der Werf, and J. Wilson: Emissions of primary aerosol and precursor gases  
921 in the years 2000 and 1750 prescribed data-sets for AeroCom: *Atmos. Chem. Phys.*,  
922 6, 4321-4344, 2006.

923 Diner, D. J., J. C. Beckert, T. H. Reilly, C. J. Bruegge, J. E. Conel, R. A. Kahn, J. V.  
924 Martonchik, T. P. Ackerman, R. Davies, S. A. W. Gerstl, H. R. Gordon, J. P. Muller,  
925 R. B. Myneni, P. J. Sellers, B. Pinty, and M. M. Verstraete: Multi-angle Imaging  
926 SpectroRadiometer (MISR) Instrument Description and Experiment Overview, *IEEE*  
927 *Trans, Geosci. Remote Sens*, 36, 1072-1087, 1998.

928 Dubovik, O. and King, M. D.: A flexible inversion algorithm for retrieval of aerosol  
929 optical properties from Sun and sky radiance measurements, *J. Geophys. Res.*,  
930 105(16), 20673-20696, 2000.

931 Dubovik, O., B. N. Holben, T. Lapyonok, A. Sinyuk, M. I. Mishchenko, P. Yang, and I.  
932 Slutsker: Non-spherical aerosol retrieval method employing light scattering by  
933 spheroids, *Geophys. Res. Lett.*, 29(10), 1415, 10.1029/2001GL014506, 2002.

934 Easter, R. C., Ghan, S. J., Zhang, Y., Saylor, R. D., Chapman, E. G., Laulainen, N. S.,  
935 Abdul-Razzak, H., Leung, L. R., Bian, X., and Zaveri, R. A.: MIRAGE: Model  
936 Description and Evaluation of Aerosols and Trace Gases, *J. Geophys. Res.*, 109,  
937 D20210, doi:10.1029/2004JD004571, 2004.

938 Eck, T. F., B. N. Holben, J. S. Reid, O. Dubovik, A. Smirnov, N. T. O'Neill, I. Slutsker,  
939 and S. Kinn: Wavelength dependence of the optical depth of biomass burning urban,  
940 and desert dust aerosols, *J. Geophys. Res.*, 104(24), 31333-31349, 1999.

941 Eguchi, K., I. Uno, K. Yumimoto, T. Takemura, A. Shimizu, N. Sugimoto, and Z. Liu:  
942 Trans-pacific dust transport: integrated analysis of NASA/CALIPSO and a global  
943 aerosol transport model, *Atmos. Chem. Phys.*, 9, 3137–3145, 2009.

944 Fairlie, T. D., D. J. Jacob, and R. J. Park: The impact of transpacific transport of mineral  
945 dust in the United States: *Atmospheric Environment*, 41, 1251-1266, 2007.

946 Fan, J., L. R. Leung, P. J. DeMott, J. M. Comstock, B. Singh, D. Rosenfeld, J. M.  
947 Tomlinson, A. White, K. A. Prather, P. Minnis, J. K. Ayers, and Q. Min: Aerosol  
948 impacts on California winter clouds and precipitation during CalWater 2011: local  
949 pollution versus long-range transported dust, *Atmos. Chem. Phys.*, 14, 81–101,  
950 doi:10.5194/acp-14-81-2014, 2014.

951 Fan, J., D. Rosenfeld, Y. Yang, C. Zhao, L. R. Leung, and Z. Li: Substantial contribution  
952 of anthropogenic air pollution to catastrophic floods in Southwest China, *Geophys.*  
953 *Res. Lett.*, 42, 6066-6075, doi:10.1002/2015GL064479, 2015.

954 Fast, J. D., W. I. Gustafson, R. C. Easter, R. A. Zaveri, J. C. Barnard, E. G. Chapman, G.  
955 A. Grell, and S. E. Peckham: Evolution of ozone, particulates, and aerosol direct  
956 radiative forcing in the vicinity of Houston using a fully coupled meteorology-  
957 chemistry- aerosol model, *J. Geophys. Res.*, 111, D21305,  
958 doi:10.1029/2005JD006721, 2006.

959 Fast, J., A. C. Aiken, J. Allan, L. Alexander, T. Campos, M. R. Canagaratna, E.  
960 Chapman, P. F. DeCarlo, B. de Foy, J. Gaffney, J. de Gouw, J. C. Doran, L. Emmons,  
961 A. Hodzic, S. C. Herndon, G. Huey, J. T. Jayne, J. L. Jimenez, L. Kleinman, W.  
962 Kuster, N. Marley, L. Russell, C. Ochoa, T. B. Onasch, M. Pekour, C. Song, I. M.  
963 Ulbrich, C. Warneke, D. Welsh-Bon, C. Wiedinmyer, D. R. Worsnop, X. Y. Yu, and  
964 R. Zaveri: Evaluating simulated primary anthropogenic and biomass burning organic  
965 aerosols during MILAGRO: implications for assessing treatments of secondary  
966 organic aerosols, *Atmos. Chem. Phys.*, 9, 6191–6215, 2009.

967 Fast, J. D., J. Allan, R. Bahreini, J. Craven, L. Emmons, R. Ferrare, P. L. Hayes, A.  
968 Hodzic, J. Holloway, C. Hostetler, J. L. Jimenez, H. Jonsson, S. Liu, Y. Liu, A.  
969 Metcalf, A. Middlebrook, J. Nowak, M. Pekour, A. Perring, L. Russell, A. Sedlacek,  
970 J. Seinfeld, A. Setyan, J. Shilling, M. Shrivastava, S. Springston, C. Song, R.  
971 Subramanian, J. W. Taylor, V. Vinoj, Q. Yang, R. A. Zaveri, and Q. Zhang:  
972 Modeling regional aerosol and aerosol precursor variability over California and its  
973 sensitivity to emissions and long-range transport during the 2010 CalNex and CARES  
974 campaigns, *Atmos. Chem. Phys.*, 14, 10013–10060, doi:10.5194/acp-14-10013-2014,  
975 2014.

976 Fischer, E. V., N. C. Hsu, D. A. Jaffe, M.-J. Jeong, and S. L. Gong: A decade of dust:  
977 Asian dust and springtime aerosol load in the U.S. Pacific Northwest, *Geophys. Res.*  
978 *Lett.*, 36, L03821, doi:10.1029/2008GL036467, 2009.

979 Fonseca, R. M., T. Zhang, and K.-T. Yong: Improved simulation of precipitation in the  
980 tropics using a modified BMJ scheme in the WRF model, *Geosci. Model Dev.*, 8,  
981 2915–2928, 2015.

982 Forster, C., O. Cooper, A. Stohl, S. Eckhardt, P. James, E. Dunlea, D. K. Nicks, J. S.  
983 Holloway, G. Hubler, D. D. Parrish, T. B. Ryerson, and M. Trainer: Lagrangian  
984 transport model forecasts and a transport climatology for the Intercontinental  
985 Transport and Chemical Transformation 2002 (ITCT 2K2) measurement campaign, *J.*  
986 *Geophys. Res.*, 109, D07S92, doi:10.1029/2003JD003589, 2004.

987 Gao, Y., X. Liu, C. Zhao, and M. Zhang: Emission controls versus meteorological  
988 conditions in determining aerosol concentrations in Beijing during the 2008 Olympic  
989 Games, *Atmos. Chem. Phys.*, 11, 12437–12451, doi:10.5194/acp-11-12437-2011,  
990 2011.

991 Gao, Y., C. Zhao, X. H. Liu, M. G. Zhang, and L. R. Leung: WRF-Chem simulations of  
992 aerosols and anthropogenic aerosol radiative forcing in East Asia, *Atmospheric*  
993 *Environment*, 92, 250-266, 2014.

994 Ginoux, P., M. Chin, I. Tegen, J. M. Prospero, B. Holben, O. Dubovik, and S. J. Lin:  
995 Sources and distributions of dust aerosols simulated with the GOCART model, *J.*  
996 *Geophys. Res.*, 106(17), 20255-20273, 2001.

997 Gong, S. L.: A parameterization of sea-salt aerosol source function for sub- and super-  
998 micron particles, *Global Biogeochemical Cycle*, 17(4), 1097,  
999 doi:10.1029/2003GB002079, 2003.

1000 Grell, G. A., S. E. Peckham, R. Schmitz, S. A. McKeen, G. Frost, W. C. Skamarock, and  
1001 B. Eder: Fully coupled “online” chemistry within the WRF model, *Atmospheric*  
1002 *Environment*, 39, 6957-6957, doi:10.1016/j.atmosenv.2005.04.027, 2005.

1003 Gustafson, W. I., E. G. Chapman, S. J. Ghan, R. C. Easter, and J. D. Fast: Impact on  
1004 modeled cloud characteristics due to simplified treatment of uniform cloud  
1005 condensation nuclei during NEAQS 2004, *Geophys. Res. Lett.*, 34, L19809,  
1006 doi:10.1029/2007GL030021, 2007.

1007 Guenther, A; Zimmerman, P; & Wildermuth, M.: Natural volatile organic compound  
1008 emission rate estimates for U.S. woodland landscapes. *Atmospheric Environment*,  
1009 28(6), 1197 - 1210. doi: 10.1016/1352-2310(94)90297-6, 1994.

1010 Hadley, O. L., V. Ramanathan, G. R. Carmichael, Y. Tang, C. E. Corrigan, G. C.  
1011 Roberts, and G. S. Mauger: Trans-Pacific transport of black carbon and fine aerosols  
1012 ( $D < 2.5 \text{ mm}$ ) into North America, *J. Geophys. Res.*, 112, D05309,  
1013 doi:10.1029/2006JD007632, 2007.

1014 Hadley, O. L., C. E. Corrigan, T. W. Kirchstetter, S. S. Cliff, and V. Ramanathan:  
1015 Measured black carbon deposition on the Sierra Nevada snow pack and implication  
1016 for snow pack retreat, *Atmos. Chem. Phys.*, 10, 7505-7513, doi:10.5194/acp-10-  
1017 7505-2010, 2010.

1018 Hagos, S. M., Z. Feng, C. D. Burleyson, C. Zhao, M. N. Martini, and L. K. Berg: Moist  
1019 Process Biases in Simulations of the Madden–Julian Oscillation Episodes Observed

1020 during the AMIE/DYNAMO Field Campaign, *J. Climate*, DOI:  
1021 <http://dx.doi.org/10.1175/JCLI-D-15-0349.1>, 2016.

1022 Hand, J., S. A. Copeland, D. E. Day, A. M. Dillner, H. Indresand, W. C. Malm, C. E.  
1023 McDade, C. T. Moore, Jr, M. L. Pitchford, B. A. Schichtel, and J. G. Watson: Spatial  
1024 and seasonal patterns and temporal variability of haze and its constituents in the  
1025 United States: Report V, June, 2011, available from  
1026 [http://vista.cira.colostate.edu/improve/Publications/ Reports/2011/2011.htm](http://vista.cira.colostate.edu/improve/Publications/Reports/2011/2011.htm), 2011.

1027 Heald, C. L., D. J. Jacob, R. J. Park, B. Alexander, T. D. Fairlie, R. M. Yantosca, and D.  
1028 A. Chu: Transpacific transport of Asian anthropogenic aerosols and its impact on  
1029 surface air quality in the United States, *J. Geophys. Res.*, 111, D14310,  
1030 doi:10.1029/2005JD006847, 2006.

1031 Hess, M., P. Koepke, and I. Schult: Optical Properties of Aerosols and Clouds: The  
1032 Software Package OPAC, *Bull. Am. Meteorol. Soc.*, 79(5), 831-844, 1998.

1033 Holben, B. N., T. F. Eck, I. Slutsker, D. Tanre', J. P. Buis, A. Setzer, E. Vermote, J. A.  
1034 Reagan, Y. J. Kaufman, T. Nakajima, F. Lavenue, I. Jankowiak, and A. Smirnov:  
1035 AERONET - A Federated Instrument Network and Data Archive for Aerosol  
1036 Characterization, *Remote Sens. Environ.*, 66, 1-16, 1998.

1037 Holben, B. N., D. Tanr, A. Smirnov, T. F. Eck, I. Slutsker, N. Abuhassan, W. W.  
1038 Newcomb, J. S. Schafer, B. Chatenet, F. Lavenue, Y. J.Kaufman, J. V. Castle, A.  
1039 Setzer, B. Markham, D. Clark, R. Frouin, R. Halthore, A. Karneli, N. T. O'Neill, C.  
1040 Pietras, R. T. Pinker, K. Voss, and G. Zibordi: An emergingsground-  
1041 basedaerosolclimatology: Aerosol optical depth from AERONET, *J. Geophys. Res.*,  
1042 106(11), 12067-12097, 2001.

1043 Hsu, N. C., S. C. Tsay, M. D. King, and J. R. Herman: Deep Blue Retrievals of Asian  
1044 Aerosol Properties During ACE-Asia, *IEEE Trans, Geosci. Remote Sens.*, 44(11),  
1045 3180-3195, 2006.

1046 Hsu, N. C., M.-J. Jeong, and C. Bettenhausen: Enhanced Deep Blue aerosol retrieval  
1047 algorithm: The second generation, *J. Geophys. Res. Atmos.*, 118 (16): 9296–9315,  
1048 2013.

1049 Hu, Y., M. Vaughan, Z. Liu, B. Lin, P. Yang, D. Flittner, B. Hunt, R. Kuehn, J. Huang,  
1050 D. Wu, S. Rodier, K. Powell, C. Trepte, and D. Winker, The depolarization-  
1051 attenuated backscatter relation: CALIPSO lidar measurements vs. theory, *Optics*  
1052 *Express*, 15 (9), 5327-5332, 2007.

1053 Hu, Y., D. Winker, M. Vaughan, B. Lin, A. Omar, C. Trepte, D. Flittner, P. Yang, S.  
1054 Nasiri, B. Baum, W. Sun, Z. Liu, Z. Wang, S. Young, K. Stamnes, J. Huang, R.  
1055 Kuehn, and R. Holz, CALIPSO/CALIOP cloud phase discrimination algorithm,  
1056 *Journal of Atmospheric and Oceanic Technology*, 26 (11) (2009), 2293-2309,  
1057 doi:10.1175/2009JTECHA1280.1, 2009.

1058 Huang, J., B. Lin, P. Minnis, T. Wang, X. Wang, Y. Hu, Y. Yi, and J. Ayers, Satellite-  
1059 based assessment of possible dust aerosols semi-direct effect on cloud water path over  
1060 East Asia, *Geophysical Research Letters*, 33 (19), L19802,  
1061 doi:10.1029/2006GL026561, 2006.

1062 Huang, J., P. Minnis, B. Chen, Z. Huang, Z. Liu, Q. Zhao, Y. Yi, and J. Ayers, Long-  
1063 range transport and vertical structure of Asian dust from CALIPSO and surface  
1064 measurements during PACDEX, *Journal of Geophysical Research*, 113 (D23),  
1065 D23212, doi:10.1029/2008JD010620, 2008.

1066 Huang, J., T. Wang, W. Wang, Z. Li, and H. Yan, 2014: Climate effects of dust aerosols  
1067 over East Asian arid and semiarid regions, *Journal of Geophysical Research:*  
1068 *Atmospheres*, 119, 11398–11416, doi:10.1002/2014JD021796, 2014.

1069 Huang, L., J. H. Jiang, J. L. Tackett, H. Su, and R. Fu: Seasonal and diurnal variations of  
1070 aerosol extinction profile and type distribution from CALIPSO 5-year observations, *J.*  
1071 *Geophys. Res. Atmos.*, 118, 4572–4596, doi:10.1002/jgrd.50407, 2013.

1072 Huffman, G. J., R. F. Adler, M. M. Morrissey, D. T. Bolvin, S. Curtis, R. Joyce, B.  
1073 McGavock, and J. Susskind: Global Precipitation at One-Degree Daily Resolution  
1074 from Multisatellite Observations. *J. Hydrometeor.*, 2, 36–50,doi:  
1075 [http://dx.doi.org/10.1175/1525-7541\(2001\)002<0036:GPAODD>2.0.CO;2](http://dx.doi.org/10.1175/1525-7541(2001)002<0036:GPAODD>2.0.CO;2), 2001.

1076 Iacono, M. J., E. J. Mlawer, S. A. Clough, and J. J. Morcrette: Impact of an  
1077 improved longwave radiation model, RRTM, on the energy budget and thermodynamic  
1078 properties of the NCAR community climate model, CCM3, *J. Geophys. Res.*,  
1079 105(11), 14873-14890, 2000.

1080 Jaegle, L., P. K. Quinn, T. S. Bates, B. Alexander, and J. T. Lin: Global distribution of  
1081 sea salt aerosols: new constraints from in situ and remote sensing observations,  
1082 *Atmos. Chem. Phys.*, 11, 3137-3157, doi:10.5194/acp-11-3137-2011, 2011.

1083 Jaffe, D., T. Anderson, D. Covert, R. Kotchenruther, B. Trost, J. Danielson, W. Simpson,  
1084 T. Berntsen, S. Karlsdottir, D. Blake, J. Harris, G. Carmichael, and I. Uno: Transport  
1085 of Asian Air Pollution to North America, *Geophys. Res. Lett.*, 26(6), 711-714, 1999.

1086 Janssens-Maenhout, G., Crippa, M., Guizzardi, D., Dentener, F., Muntean, M., Pouliot,  
1087 G., Keating, T., Zhang, Q., Kurokawa, J., Wankmüller, R., Denier van der Gon, H.,  
1088 Kuenen, J. J. P., Klimont, Z., Frost, G., Darras, S., Koffi, B., and Li, M.: HTAP\_v2.2:

1089 a mosaic of regional and global emission grid maps for 2008 and 2010 to study  
1090 hemispheric transport of air pollution, *Atmos. Chem. Phys.*, 15, 11411-11432,  
1091 doi:10.5194/acp-15-11411-2015, 2015.

1092 Jethva, H., O. Torres, and C. Ahn: Global assessment of OMI aerosol single-scattering  
1093 albedo using ground-based AERONET inversion, *J. Geophys. Res. Atmos.*, 119,  
1094 9020–9040, doi:10.1002/2014JD021672, 2014.

1095 Kahn, R. A., D. L. Nelson, M. J. Garay, R. C. Levy, M. A. Bull, D. J. Diner, J. V.  
1096 Martonchik, S. R. Paradise, E. G. Hansen, and L. A. Remer: MISR Aerosol Product  
1097 Attributes and Statistical Comparisons With MODIS, *IEEE Trans, Geosci. Remote*  
1098 *Sens*, 47(12), 4095-4114, 2009.

1099 Kaufman, Y. J., D. Tanré, L. A. Remer, E. F. Vermote, A. Chu, and B. N. Holben:  
1100 Operational remote sensing of tropospheric aerosol over land from EOS moderate  
1101 resolution imaging spectroradiometer, *J. Geophys. Res.*, 102(D14), 17051-17067,  
1102 1997.

1103 Kaufman, Y. J., O. Boucher, D. Tanre, M. Chin, L. A. Remer, and T. Takemura: Aerosol  
1104 anthropogenic component estimated from satellite data, *Geophys. Res. Lett.*, 32,  
1105 L17804, doi:10.1029/2005GL023125, 2005a.

1106 Kaufman, Y. J., I. Koren, L. A. Remer, D. Rosenfeld, and Y. Rudich: The effect of  
1107 smoke, dust, and pollution aerosol on shallow cloud development over the Atlantic  
1108 Ocean, *Proc. Natl. Acad. Sci. USA*, 102(32), 11207-11212,  
1109 Doi/10.1073/pnas.0505191102, 2005b.

1110 King, M. D., Y. J. Kaufman, D. Tanre, and T. Nakajima: Remote Sensing of  
1111 Tropospheric Aerosols from Space: Past, Present, and Future, *Bull. Am. Meteorol.*  
1112 *Soc.*, 80(11), 2229-2259, 1999.

1113 Kok, J. F.: A scaling theory for the size distribution of emitted dust aerosols suggests  
1114 climate models underestimate the size of the global dust cycle, *Proc. Natl. Acad. Sci.*  
1115 *USA*, 108(3), 1016-1021, doi/10.1073/pnas.1014798108, 2011.

1116 Koren, I., Y. J. Kaufman, D. Rosenfeld, L. A. Remer, and Y. Rudich: Aerosol  
1117 invigoration and restructuring of Atlantic convective clouds, *Geophys. Res. Lett.*, 2,  
1118 L14828, doi:10.1029/2005GL023187, 2005.

1119 Lau, K., V. Ramanathan, G. Wu, Z. Li, S. Tsay, C. Hsu, R. Sikka, B. Holben, D. Lu, G.  
1120 Tartari, M. Chin, P. Koudelova, H. Chen, Y. Ma, J. Huang, K. Taniguchi, and R.  
1121 Zhang, The joint aerosol-monsoon experiment: A new challenge for monsoon climate  
1122 research, *Bulletin of American Meteorological Society*, 89 (3), 369-383, 2008.

1123 Levy, R. C., L. A. Remer, R. G. Keidman, S. Mattoo, C. Ichoku, R. Kahn, and T. F. Eck:  
1124 Global evaluation of the Collection 5 MODIS dark-target aerosol products over land,  
1125 *Atmos. Chem. Phys.*, 10, 10399–10420, doi:10.5194/acp-10-10399-2010, 2010.

1126 Levy, R. C., S. Mattoo, L. A. Munchak, L. A. Remer, A. M. Sayer, F. Patadia, and N.  
1127 Hsu: The Collection 6 MODIS Aerosol Products over Land and Ocean, *Atmos. Meas.*  
1128 *Tech.*, 6, 2989-3034 doi:10.5194/amt-6-2989-2013, 2013.

1129 Li, M., Q. Zhang, J. Kurokawa, J. H. Woo, K. B. He, Z. Lu, T. Ohara, Y. Song, D. G.  
1130 Streets, G. R. Carmichael, Y. F. Cheng, C. P. Hong, H. Huo, X. J. Jiang, S. C. Kang,  
1131 F. Liu, H. Su, and B. Zheng (2015), MIX: a mosaic Asian anthropogenic emission

1132 inventory for the MICS-Asia and the HTAP projects, *Atmos. Chem. Phys. Discuss.*,  
1133 15(23), 34813-34869, doi:10.5194/acpd-15-34813-2015.

1134 Liang, Q., L. Jaegle, D. A. Jaffe, P. Weiss-Penzias, A. Heckman, and J. A. Snow: Long-  
1135 range transport of Asian pollution to the northeast Pacific: Seasonal variations and  
1136 transport pathways of carbon monoxide, *J. Geophys. Res.*, 109, D23S07,  
1137 doi:10.1029/2003JD004402, 2004.

1138 Liu, Z., M. A. Vaughan, D. M. Winker, C. A. Hostetler, L. R. Poole, D. Hlavka, W. Hart,  
1139 and M. McGill: Use of probability distribution functions for discriminating between  
1140 cloud and aerosol in lidar backscatter data, *J. Geophys. Res.*, 109, D15202,  
1141 doi:10.1029/2004JD004732, 2004.

1142 Liu, Z., D. Liu, J. Huang, M. Vaughan, I. Uno, N. Sugimoto, C. Kittaka, C. Trepte, Z.  
1143 Wang, C. Hostetler, and D. Winker, Airborne dust distributions over the Tibetan  
1144 Plateau and surrounding areas derived from the first year of CALIPSO lidar  
1145 observations, *Atmospheric Chemistry and Physics*, 8 (16), 5045-5060, 2008.

1146 Lu, Z., Q. Zhang, and D. G. Streets: Sulfur dioxide and primary carbonaceous aerosol  
1147 emissions in China and India, 1996–2010, *Atmos. Chem. Phys.*, 11, 9839-9864,  
1148 doi:10.5194/acp-11-9839-2011, 2011.

1149 Malm, W. C., J. F. Sisler, D. Huffman, R. A. Eldred, and T. A. Cahill: Spatial and  
1150 seasonal trends in particle concentration and optical extinction in the United States,  
1151 99(D1), 1347-1370, 1994.

1152 Mao, Y. H., Li, Q. B., Zhang, L., Chen, Y., Randerson, J. T., Chen, D., and Liou, K. N.:  
1153 Biomass burning contribution to black carbon in the Western United States Mountain

1154 Ranges, *Atmos. Chem. Phys.*, 11, 11253–11266, doi:10.5194/acp-11- 11253-2011,  
1155 2011.

1156 Mao, Y. H., Li, Q. B., Chen, D., Zhang, L., Hao, W.-M., and Liou, K.-N.: Top-down  
1157 estimates of biomass burning emissions of black carbon in the Western United States,  
1158 *Atmos. Chem. Phys.*, 14, 7195-7211, doi:10.5194/acp-14-7195-2014, 2014.

1159 Martonchik, J. V., David J. D., Kathleen A. C., and M. A. Bull: Regional Aerosol  
1160 Retrieval Results From MISR, *IEEE Trans, Geosci. Remote Sens*, 40(7), 1520-1531,  
1161 2002.

1162 McKeen, S. A., G. Wotawa, D. D. Parrish, J. S. Holloway, M. P. Buhr, G. Hubler, F. C.  
1163 Fehsenfeld, and J. F. Meagher: Ozone production from Canadian wildfires during  
1164 June and July of 1995, *J. Geophys. Res.*, 107(D14), 4192, 10.1029/2001JD000697,  
1165 2002.

1166 Mlawer, E. J., S. J. Taubman, P. D. Brown, M. J. Iacono, and S. A. Clough: Radiative  
1167 transfer for inhomogeneous atmospheres: RRTM, a validated correlated-k model for  
1168 the longwave, *J. Geophys. Res.*, 102(D14), 16663-16682, 1997.

1169 Painter, T. H., J. S. Deems, J. Belnap, A. F. Hamlet, C. C. Landry, and B. Udall:  
1170 Response of Colorado River runoff to dust radiative forcing in snow, *Proc. Natl.*  
1171 *Acad. Sci. USA*, 107(40), 17125-17130, doi/10.1073/pnas.0913139107, 2010.

1172 Penner, J. E., S. Y. Zhang, M. Chin, C. C. Chuang, J. Fechter, Y. Feng, I. V.  
1173 Geogdzhayev, P. Ginoux, M. Herzog, A. Higurashi, D. Koch, C. Land, U. Lohmann,  
1174 M. Mischecko, T. Nakajima, G. Pitari, B. Soden, I. Tegen, and L. Stowe: A  
1175 Comparison of Model- and Satellite-Derived Aerosol Optical Depth and Reflectivity,  
1176 *J. Atmos. Sci.*, 59, 441-460, 2002.

1177 Qian, Y., W. I. Gustafson, L. R. Leung, and S. J. Ghan: Effects of soot-induced snow  
1178 albedo change on snowpack and hydrological cycle in western United States based on  
1179 Weather Research and Forecasting chemistry and regional climate simulations, *J.*  
1180 *Geophys. Res.*, 114, D03108, doi:10.1029/2008JD011039, 2009.

1181 Qian, Y., W. I. Gustafson Jr. and J. D. Fast: An investigation of the sub-grid variability of  
1182 trace gases and aerosols for global climate modeling, *Atmos. Chem. Phys.*, 10, 6917-  
1183 6946, doi:10.5194/acp-10-6917-2010, 2010.

1184 Qian, Y., H. Yan, Z. Hou, C. Johannesson, S. Klein, D. Lucas, R. Neale, P. Rasch, L.  
1185 Swiler, J. Tannahill, H. Wang, M. Wang, and C. Zhao: Parametric sensitivity analysis  
1186 of precipitation at global and local scales in the Community Atmosphere Model  
1187 CAM5, *J. Adv. Model. Earth Syst.*, 7, 382-411, doi:10.1002/2014MS000354, 2015.

1188 Remer, L. A., Y. J. Kaufman, D. Tanre, S. Mattoo, D. A. Chu, J. V. Martins, R. R. Li, C.  
1189 Ichoku, R. C. Levy, R. G. Kleidman, T. F. Eck, E. Vermote, and B. N. Holben: The  
1190 MODIS aerosol algorithm, products and validation, *J. Atmos. Sci.*, 62, 947-973,  
1191 2005.

1192 Remer, L. A. and Kaufman, Y. J.: Aerosol direct radiative effect at the top of the  
1193 atmosphere over cloud free ocean derived from four years of MODIS data, *Atmos.*  
1194 *Chem. Phys.*, 6, 237–253, 2006.

1195 Rienecker, M. M., M. J. Suarez, R. Gelaro, R. Todling, J. Bacmeister, E. Liu, M. G.  
1196 Bosilovich, S. D. Schubert, L. Takacs, G.-K. Kim, S. Bloom, J. Chen, D. Collins, A.  
1197 Conaty, A. da Silva, W. Gu, J. Joiner, R. D. Koster, R. Lucchesi, A. Molod, T.  
1198 Owens, S. Pawson, P. Pegion, C. R. Redder, R. Reichle, F. R. Robertson, A. G.  
1199 Ruddick, M. Sienkiewicz, and J. Woollen: MERRA: NASA’s Modern-Era

1200 Retrospective Analysis for Research and Applications. *J. Climate*, 24, 3624–3648.  
1201 doi: <http://dx.doi.org/10.1175/JCLI-D-11-00015.1>, 2011.

1202 Sassen, K.: Indirect climate forcing over the western US from Asian Dust storm,  
1203 *Geophys. Res. Lett.*, 29(10), 1465, [10.1029/2011GL014051](https://doi.org/10.1029/2011GL014051), 2002.

1204 Schulz, M., C. Textor, S. Kinne, Y. Balkanski, S. Bauer, T. Berntsen, T. Berglen, O.  
1205 Boucher, F. Dentener, S. Guibert, I. S. A. Isaksen, T. Iversen, D. Koch, A. Kirkevåg,  
1206 X. Liu, V. Montanaro, G. Myhre, J. E. Penner, G. Pitari, S. Reddy, Ø. Seland, P.  
1207 Stier, and T. Takemura: Radiative forcing by aerosols as derived from the AeroCom  
1208 present-day and pre-industrial simulations, *Atmos. Chem. Phys.*, 6, 5225–5246, 2006.

1209 Schuster, G. L., O. Dubovik, and B. N. Holben: Angstrom exponent and bimodal aerosol  
1210 size distributions, *J. Geophys. Res.*, 111, D07207, doi:[10.1029/2005JD006328](https://doi.org/10.1029/2005JD006328), 2006.

1211 Shrivastava, M., J. Fast, R. Easter, W. I. Gustafson, R. A. Zaveri, J. L. Jimenez, P. Saide,  
1212 and A. Hodzic: Modeling organic aerosols in a megacity: comparison of simple and  
1213 complex representations of the volatility basis set approach, 11, 6639–6662,  
1214 doi:[10.5194/acp-11-6639-2011](https://doi.org/10.5194/acp-11-6639-2011), 2011.

1215 Skamarock, W. C. and Klemp, J. B.: A time-split nonhydrostatic atmospheric model for  
1216 weather research and forecasting applications, *J. Com. Phy.*, 227, 3456–3485,  
1217 doi:[10.1016/j.jcp.2007.01.037](https://doi.org/10.1016/j.jcp.2007.01.037), 2008.

1218 Smirnov, A., B. N. Holben, T. F. Eck, O. Dubovik, and I. Slutsker: Effect of wind speed  
1219 on columnar aerosol optical properties at Midway Island, *J. Geophys. Res.*, 108,  
1220 4802, doi:[10.1029/2003JD003879](https://doi.org/10.1029/2003JD003879), D24, 2003.

1221 Stauffer, D. R. and Seaman, N. L.: Use of Four-Dimensional Data Assimilation in a  
1222 Limited\_Area Mesoscale Model. Part I: Experiments with Synoptic-Scale Data, *Mon.*  
1223 *Wea. Rev.*, 118, 1250-1277, 1990.

1224 Takemura T, Nakajima T, Dubovik O, Holben BN, Kinne S. Single-scattering albedo and  
1225 radiative forcing of various aerosol species with a global three-dimensional model. *J*  
1226 *Climate*,15:333–52,2002.

1227 Tao, Z., H. Yu, and M. Chin, Impact of transpacific aerosol on air quality over the United  
1228 States: A perspective from aerosol-cloud-radiation interactions, *Atmos. Environ.*,  
1229 125, 48-60, 2016.

1230 Textor, C., M. Schulz, S. Guibert, S. Kinne, Y. Balkanski, S. Bauer, T. Berntsen, T.  
1231 Berglen, O. Boucher, M. Chin, F. Dentener, T. Diehl, R. Easter, H. Feichter, D.  
1232 Fillmore, S. Ghan, P. Ginoux, S. Gong, A. Grini, J. Hendricks, L. Horowitz, P.  
1233 Huang, I. Isaksen, T. Iversen, S. Kloster, D. Koch, A. Kirkevag, J. E. Kristjansson,  
1234 M. Krol, A. Lauer, J. F. Lamarque, X. Liu, V. Montanaro, G. Myhre, J. Penner, G.  
1235 Pitari, S. Reddy, Ø. Seland, P. Stier, T. Takemura, and X. Tie: Analysis and  
1236 quantification of the diversities of aerosol life cycles within AeroCom, *Atmos. Chem.*  
1237 *Phys.*, 6, 1777–1813, 2006.

1238 Torres, O., C. Ahn, and Z. Chen: Improvements to the OMI near-UV aerosol algorithm  
1239 using A-train CALIOP and AIRS observations, *Atmos. Meas. Tech.*, 6, 3257–3270,  
1240 doi:10.5194/amt-6-3257-2013, 2013.

1241 Uno, I., K. Eguchi, K. Yumimoto, T. Takemura, A. Shimizu, M. Uematsu, Z. Liu, Z.  
1242 Wang, Y. Hara, and N. Sugimoto: Asian dust transported one full circuit around the  
1243 globe, *Nature Geoscience*, 557-560, doi:10.1038/ngeo583, 2009.

1244 Uno, I., Eguchi, K., Yumimoto, K., Liu, Z., Hara, Y., Sugimoto, N., Shimizu, A., and  
1245 Takemura, T.: Large Asian dust layers continuously reached North America in April  
1246 2010, *Atmos. Chem. Phys.*, 11, 7333-7341, doi:10.5194/acp-11-7333-2011, 2011.

1247 VanCuren, R. A.: Asian aerosols in North America: Extracting the chemical composition  
1248 and mass concentration of the Asian continental aerosol plume from long-term  
1249 aerosol records in the western United States, *J. Geophys. Res.*, 108, NO. D20, 4623,  
1250 doi:10.1029/2003JD003459, 2003.

1251 van der Werf, G. R., J. T. Randerson, L. Giglio, G. J. Collatz, M. Mu, P. S. Kasibhatla, D.  
1252 C. Morton, R. S. DeFries, Y. Jin, and T. T. van Leeuwen: Global fire emissions and  
1253 the contribution of deforestation, savanna, forest, agricultural, and peat fires (1997–  
1254 2009), *Atmos. Chem. Phys.*, 10, 11707–11735, doi:10.5194/acp-10-11707-2010,  
1255 2010.

1256 Veihelmann, B., P. F. Levelt, P. Stammes, and J. P. Veefkind: Simulation study of the  
1257 aerosol information content in OMI spectral reflectance measurements, *Atmos.*  
1258 *Chem. Phys.*, 7, 3115–3127, 2007.

1259 Wiedinmyer, C., S. K. Akagi, R. J. Yokelson, L. K. Emmons, J. A. Al-Saadi, J. J.  
1260 Orlando, and A. J. Soja. "The Fire Inventory from Ncar (Finn): A High Resolution  
1261 Global Model to Estimate the Emissions from Open Burning." *Geoscientific Model*  
1262 *Development* 4, no. 3 (2011): 625-41, 2011.

1263 Winker, D. M., W. H. Hunt, and M. J. McGill: Initial performance assessment of  
1264 CALIOP, *J. Geophys. Res.*, 34, L19803, doi:10.1029/2007GL030135, 2007.

1265 Winker, D. M., M. A. Vaughan, A. Omar, Y. Hu, K. A. Powell, Z. Liu, W. H. Hunt, and  
1266 S. A. Young: Overview of the CALIPSO Mission and CALIOP Data Processing

1267 Algorithms, *J. Atmos. Oceanic Technol.*, 26, 2310–2323, doi:  
1268 <http://dx.doi.org/10.1175/2009JTECHA1281.1>, 2009.

1269 Yu, H. B., R. E. Dickinson, M. Chin, Y. J. Kaufman, B. N. Holben, I. V. Geogdzhayev,  
1270 and M. I. Mishchenko: Annual cycle of global distributions of aerosol optical depth  
1271 from integration of MODIS retrievals and GOCART model simulations, *J. Geophys.*  
1272 *Res.*, 108, NO. D3, 4128, doi:10.1029/2002JD002717, 2003.

1273 Yu, H. B., R. E. Dickinson, M. Chin, Y. J. Kaufman, M. Zhou, L. Zhou, Y. Tian, O.  
1274 Dubovik, and B. N. Holben: Direct radiative effect of aerosols as determined from a  
1275 combination of MODIS retrievals and GOCART simulations, *J. Geophys. Res.*, 109,  
1276 D03206, doi:10.1029/2003JD003914, 2004.

1277 Yu, H. B., R. Fu, R. E. Dickinson, Y. Zhang, M. Chen, and H. Wang, Interannual  
1278 variability of smoke and warm cloud relationships in the Amazon as inferred from  
1279 MODIS retrievals, *Remote Sens. Environ.*, 111, 435-449,  
1280 doi:10.1016/j.rse.2007.04.003, 2007.

1281 Yu, H. B., L. A. Remer, M. Chin, H. S. Bian, R. G. Kleidman, and T. Diehl: A satellite-  
1282 based assessment of transpacific transport of pollution aerosol, *J. Geophys. Res.*, 113,  
1283 D14S12, doi:10.1029/2007JD009349, 2008.

1284 Yu, H., M. Chin, L. A. Remer, R. G. Kleidman, N. Bellouin, H. Bian, and T. Diehl:  
1285 Variability of marine aerosol fine-mode fraction and estimates of anthropogenic  
1286 aerosol component over cloud-free oceans from MODIS, *J. Geophys. Res.*, 114,  
1287 D10206, doi:10.1029/2008JD010648, 2009.

1288 Yu, H. B., M. Chin, D. M. Winker, A. H. Omar, Z. Y. Liu, C. Kittaka, and T. Diehl:  
1289 Global view of aerosol vertical distributions from CALIPSO lidar measurements and

1290 GOCART simulations: Regional and seasonal variations, *J. Geophys. Res.*, 115,  
1291 D00H30, doi:10.1029/2009JD013364, 2010.

1292 Yu, H., L. A. Remer, M. Chin, H. Bian, Q. Tan, T. Yuan, and Y. Zhang: Aerosols from  
1293 Overseas Rival Domestic Emissions over North America, *Science*, 337, 566-569,  
1294 2012.

1295 Yu, H., M. Chin, H. Bian, T. L. Yuan, J. M. Prospero, A. H. Omar, L. A. Remer, D. M.  
1296 Winker, Y. Yang, Y. Zhang, and Z. Zhang: Quantification of trans-Atlantic dust  
1297 transport from seven-year (2007-2013) record of CALIPSO lidar measurements,  
1298 *Remote Sens. Environ.*, 159, 232-249, <http://dx.doi.org/10.1016/j.rse.2014.12.010>,  
1299 2015.

1300 Zaveri, R. A. and Peters, L. K.: A new lumped structure photochemical mechanism for  
1301 large-scale applications, *J. Geophys. Res.*, 104(D23), 30387-30415, 1999.

1302 Zaveri, R. A., R. C. Easter, J. D. Fast, and L. K. Peters: Model for Simulating Aerosol  
1303 Interactions and Chemistry (MOSAIC), *J. Geophys. Res.*, 113, D13204,  
1304 doi:10.1029/2007JD008782, 2008.

1305 Zhang, J. and Reid, J. S.: MODIS aerosol product analysis for data assimilation:  
1306 Assessment of over-ocean level 2 aerosol optical thickness retrievals, *J. Geophys.*  
1307 *Res.*, 111, D22207, doi:10.1029/2005JD006898, 2006.

1308 Zhang, Q., D. G. Streets, G. R. Carmichael, K. B. He, H. Huo, A. Kannari, Z. Klimont, I.  
1309 S. Park, S. Reddy, J. S. Fu, D. Chen, L. Duan, Y. Lei, L. T. Wang, and Z. L. Yao:  
1310 Asian emissions in 2006 for the NASA INTEX-B mission, *Atmos. Chem. Phys.*, 9,  
1311 5131-5153, 2009.

1312 Zhao, C., X. Liu, L. R. Leung, B. Johnson, S. A. McFarlane, W. I. Gustafson, J. D. Fast,  
1313 and R. Easter: The spatial distribution of mineral dust and its shortwave radiative  
1314 forcing over North Africa: modeling sensitivities to dust emissions and aerosol size  
1315 treatments, *Atmos. Chem. Phys.*, 10, 8821–8838, doi:10.5194/acp-10-8821-2010,  
1316 2010a.

1317 Zhao, C., Y. Wang, Q. Yang, R. Fu, and Y. Choi: Impact of East Asia summer monsoon  
1318 on the air quality over China: view from space, *J. Geophys. Res.*, 115, D09301,  
1319 doi:10.1029/2009JD012745, 2010.

1320 Zhao, C., X. Liu, L. R. Leung, and S. Hagos: Radiative impact of mineral dust on  
1321 monsoon precipitation variability over West Africa, *Atmos. Chem. Phys.*, 11, 1879-  
1322 1893, doi:10.5194/acp-11-1879-2011, 2011.

1323 Zhao, C., X. Liu, and L. R. Leung: Impact of the Desert dust on the summer monsoon  
1324 system over Southwestern North America, *Atmos. Chem. Phys.*, 12, 3717–3731, d  
1325 oi:10.5194/acp-12-3717-2012, 2012.

1326 Zhao, C., L. R. Leung, R. Easter, J. Hand, and J. Avise: Characterization of speciated  
1327 aerosol direct radiative forcing over California, *J. Geophys. Res.*, 118, 2372–2388,  
1328 doi:10.1029/2012JD018364, 2013a.

1329 Zhao, C., S. Chen, L. R. Leung, Y. Qian, J. F. Kok, R. A. Zaveri, and J. Huang:  
1330 Uncertainty in modeling dust mass balance and radiative forcing from size  
1331 parameterization, *Atmos. Chem. Phys.*, 13, 10733–10753, doi:10.5194/acp-13-10733-  
1332 2013, 2013b.

1333 Zhao, C., Z. Hu, Y. Qian, L. R. Leung, J. Huang, M. Huang, J. Jin, M. G. Flanner, R.  
1334 Zhang, H. Wang, H. Yan, Z. Lu, and D. G. Streets: Simulating black carbon and dust

1335 and their radiative forcing in seasonal snow: a case study over North China with field  
1336 campaign measurements, *Atmos. Chem. Phys.*, 14, 11475–11491, doi:10.5194/acp-  
1337 14-11475-2014, 2014.

1338 Zhao, C., M. Huang, J. Fast, L. Berg, Y. Qian, A. Guenther, D. Gu, M. Shrivastava, Y.  
1339 Liu, S. Walters, G. Pfister, J. Jin: Sensitivity of biogenic volatile organic compounds  
1340 (BVOCs) to land surface processes and vegetation distributions in California, *Geosci.*  
1341 *Model Dev. Discuss.*, doi:10.5194/gmd-2015-266, in review, 2016.

1342

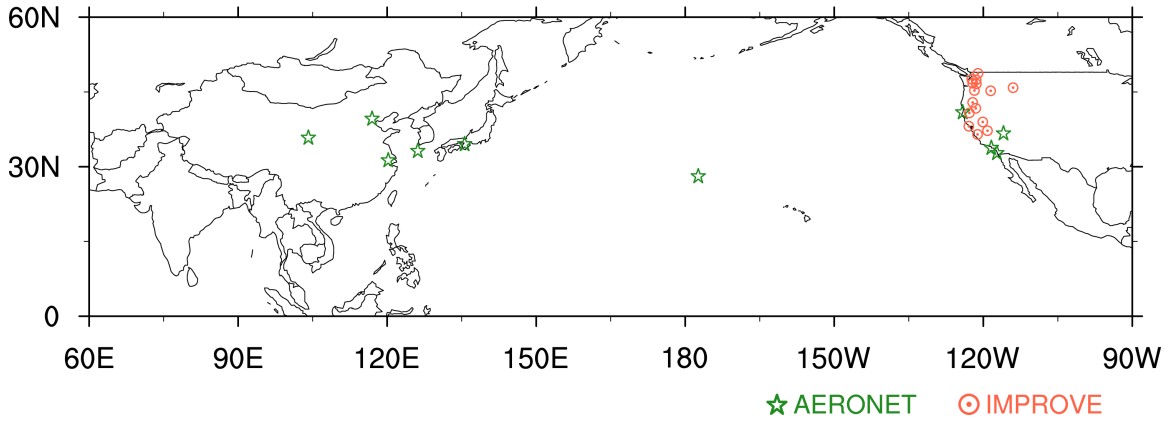
1343

1344

1345

1346

1347



1348

1349 **Figure 1** Observation sites for the AERONET (green stars) and IMPROVE (red dot

1350 circle) networks used in this study.

1351

1352

1353

1354

1355

1356

1357

1358

1359

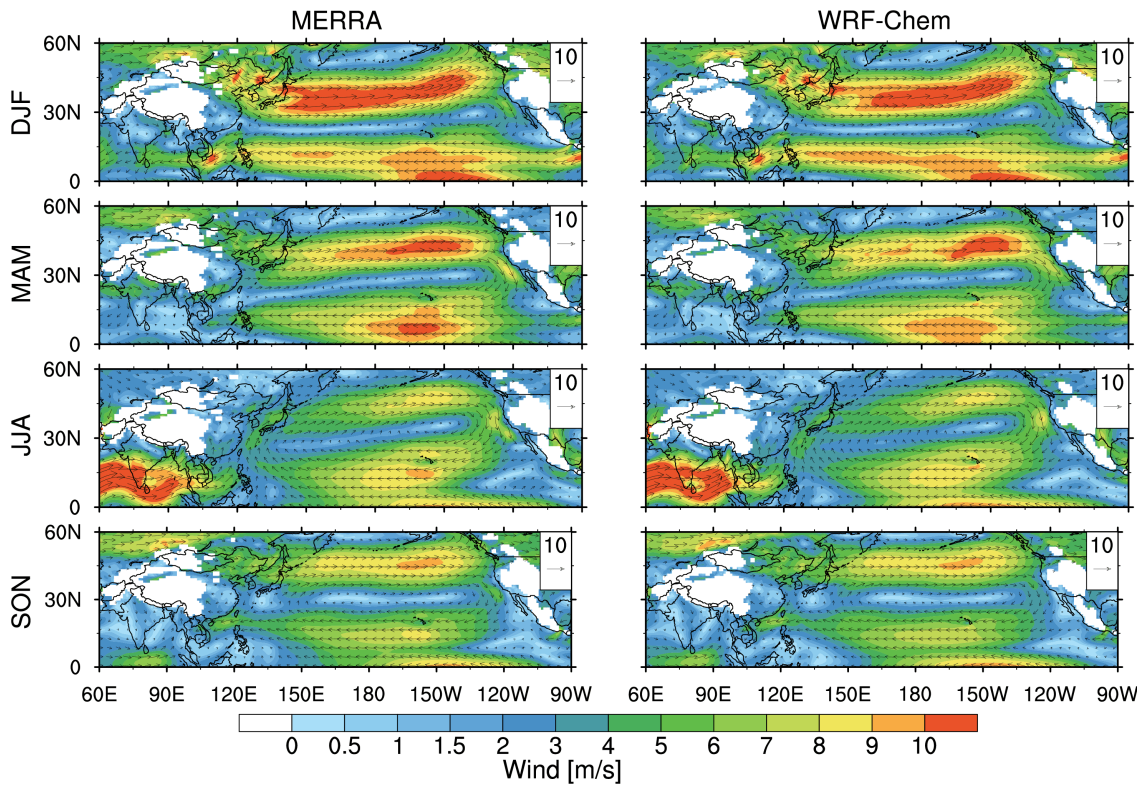
1360

1361

1362

1363

1364



1365

1366 **Figure 2** Spatial distributions of seasonal averaged wind fields at 850hPa from the

1367 MERRA reanalysis and the WRF-Chem simulation for the period 2010-2014.

1368

1369

1370

1371

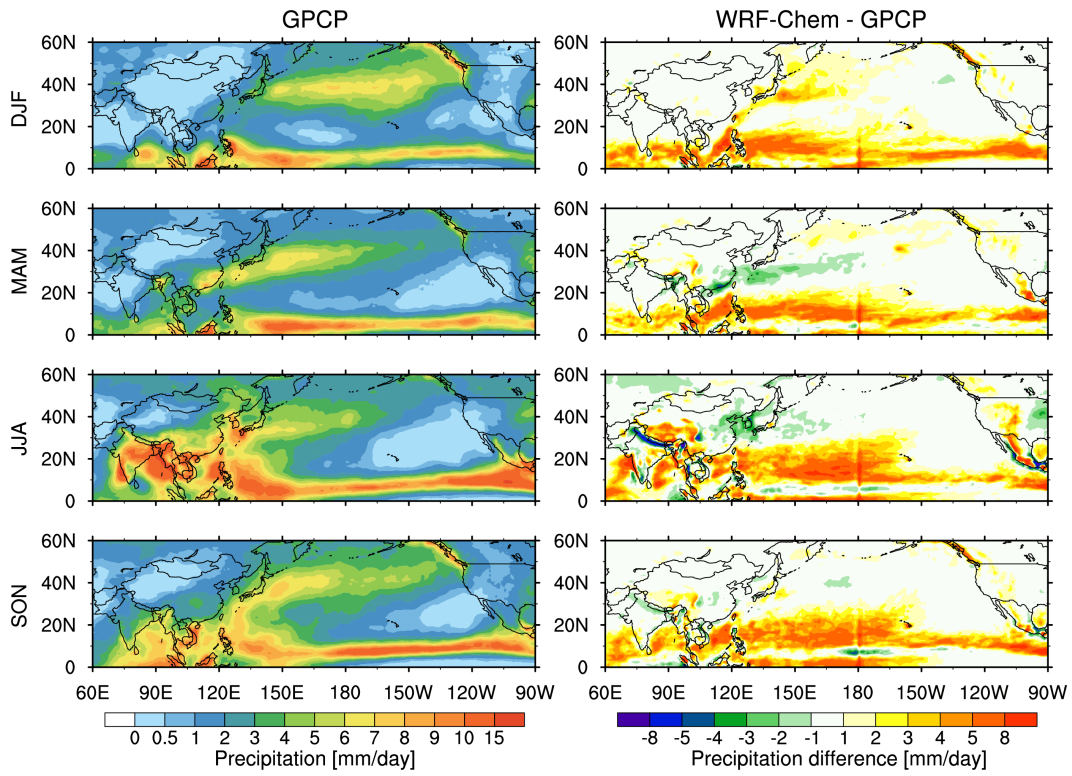
1372

1373

1374

1375

1376



1377

1378 **Figure 3** Spatial distributions of seasonal averaged precipitation from the GPCP  
1379 observation and the difference between GPCP and the WRF-Chem simulation for the  
1380 period 2010-2014.

1381

1382

1383

1384

1385

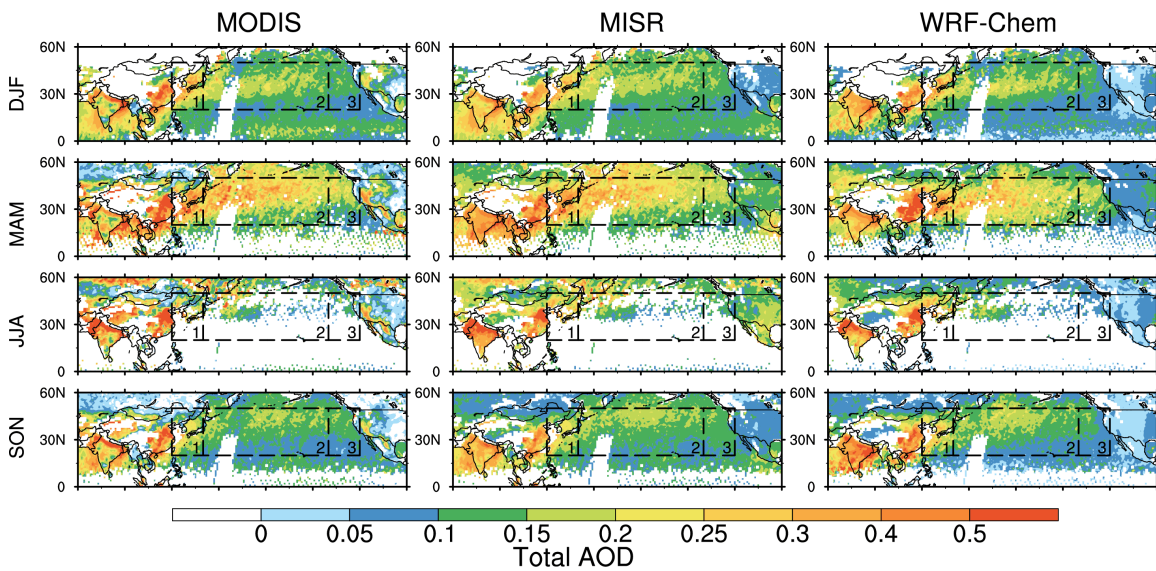
1386

1387

1388

1389

1390



1391

1392 **Figure 4** Spatial distributions of seasonal mean 550 nm AOD from the retrievals of  
1393 MODIS and MISR onboard Terra and the WRF-Chem simulation for the period 2010-  
1394 2014. The daily results from MISR, MODIS, and WRF-Chem are only sampled for  
1395 averaging when all of them have valid values at the same location and time. Three sub-  
1396 regions are denoted by the black boxes: Region 1 ( $20^{\circ}$  N- $50^{\circ}$  N and  $120^{\circ}$  E- $140^{\circ}$  E),  
1397 Region 2 ( $20^{\circ}$  N- $50^{\circ}$  N and  $140^{\circ}$  E- $140^{\circ}$  W), and Region 3 ( $20^{\circ}$  N- $50^{\circ}$  N and  $140^{\circ}$  W- $120^{\circ}$   
1398 W).

1399

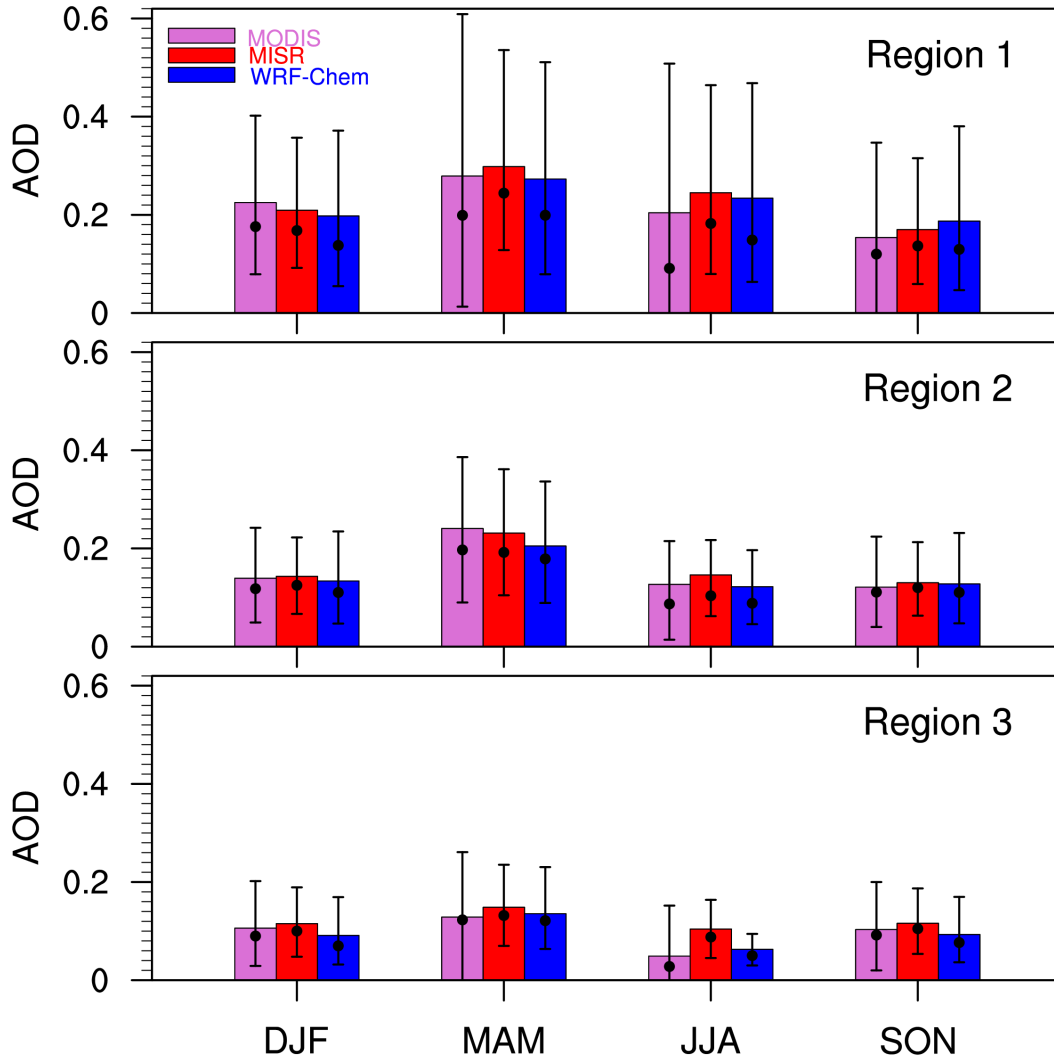
1400

1401

1402

1403

1404



1405

1406

1407

1408

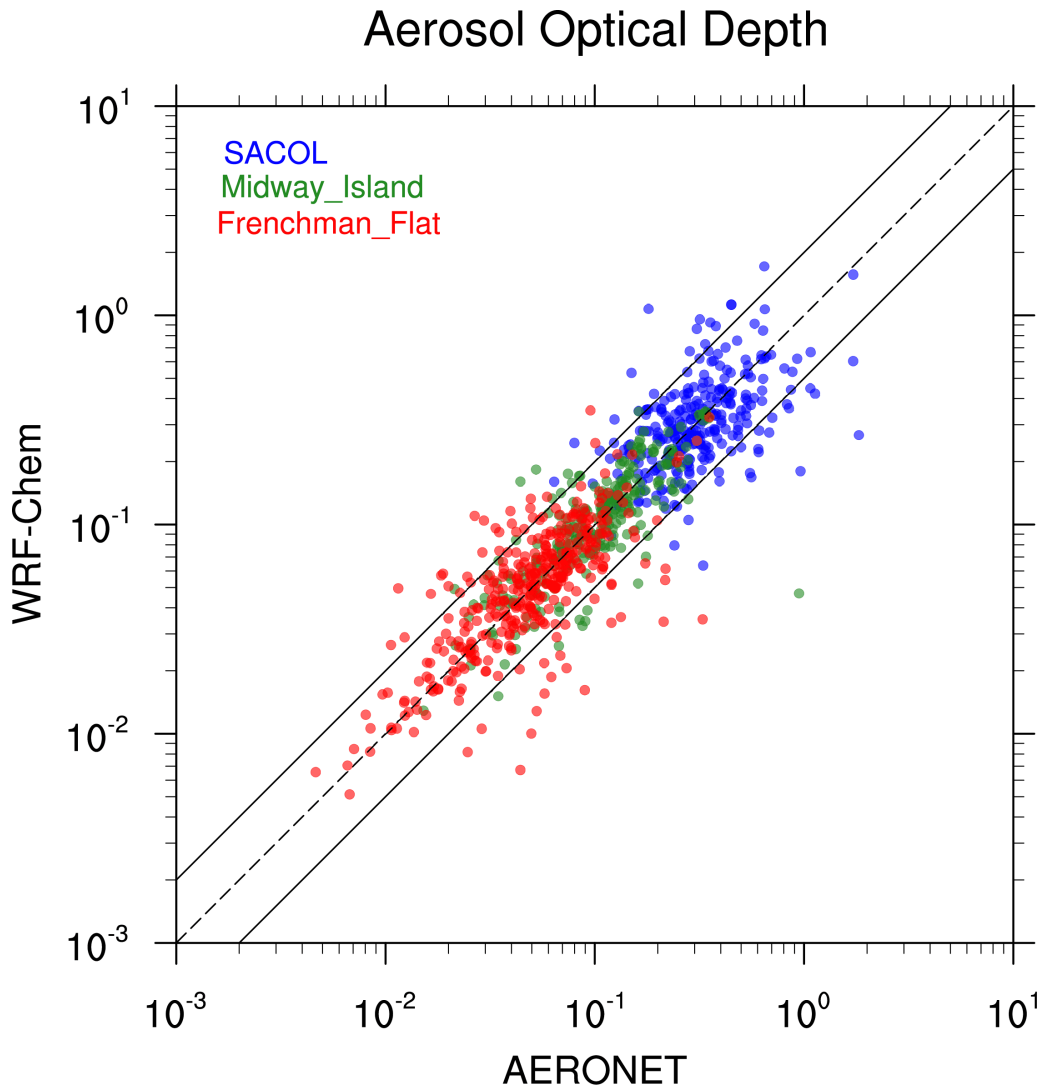
1409

1410

1411

**Figure 5** Seasonal mean 550nm AOD from MISR and MODIS retrievals, and the corresponding WRF-Chem simulation averaged for the period 2010-2014, over the three sub-regions shown in Fig. 4. The values of bars represent the mean. The vertical lines represent 10<sup>th</sup> and 90<sup>th</sup> percentile values, and the black dots represent the median values.

1412



1413

1414 **Figure 6** The AERONET observations of daily AOD at 550 nm at the three sites  
1415 (SACOL, Midway Island, and Frenchman Flat) versus the corresponding WRF-Chem  
1416 simulation for the period 2010-2014.

1417

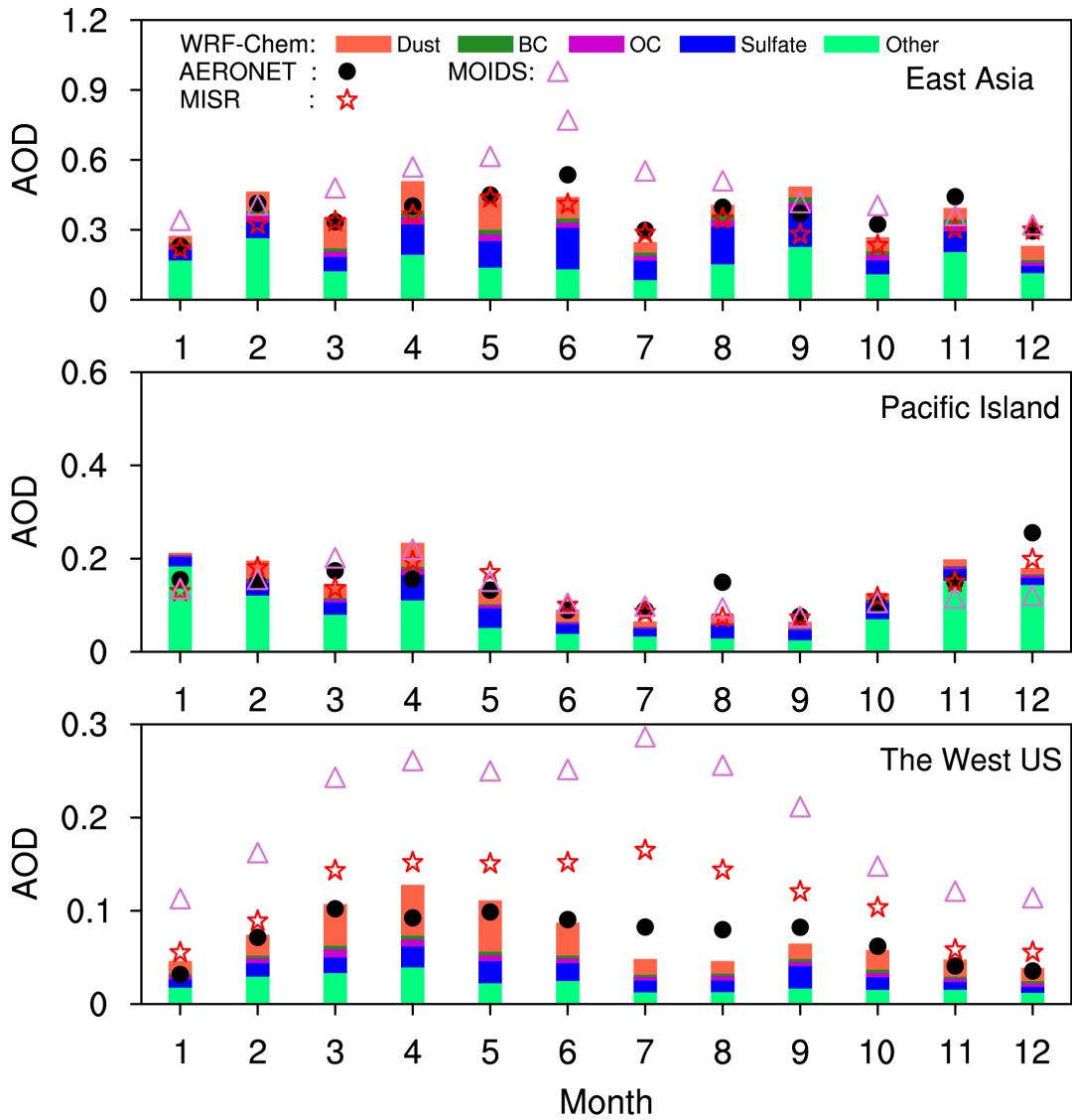
1418

1419

1420

1421

1422



1423

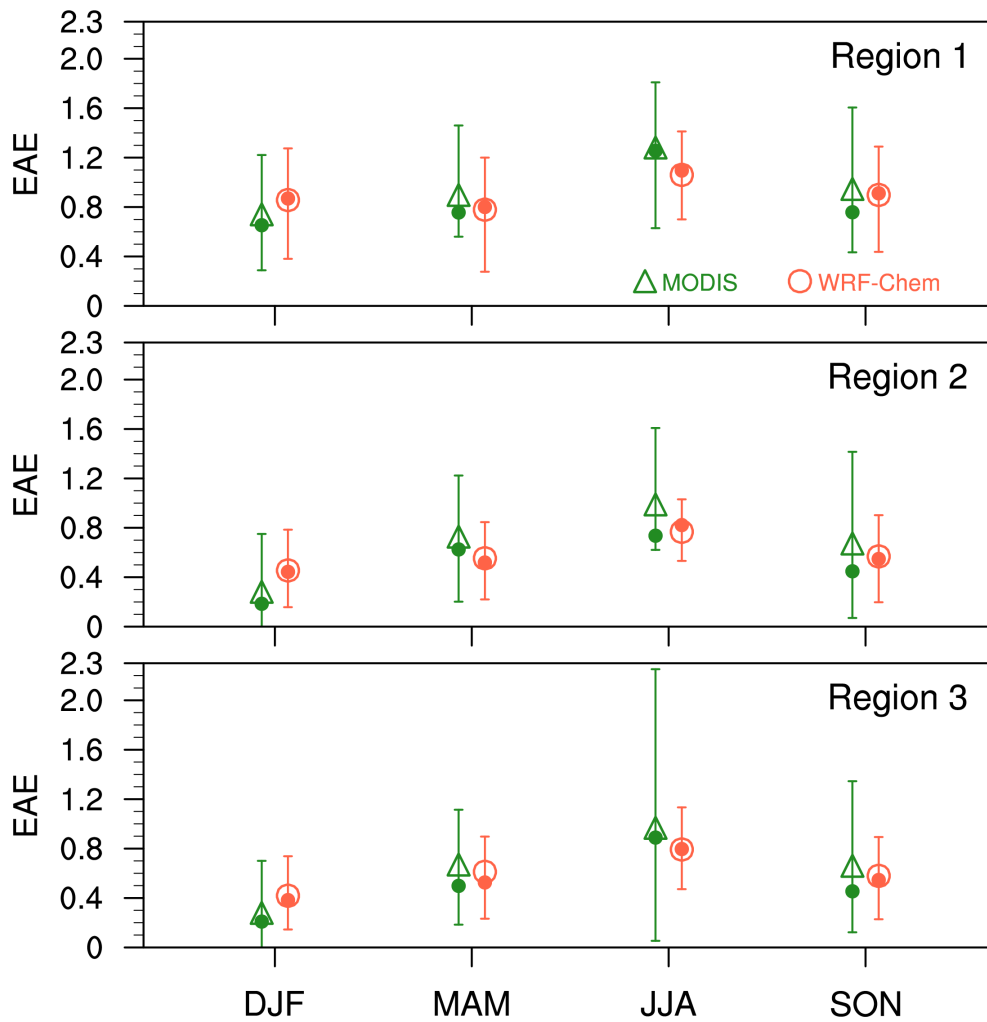
1424 **Figure 7** Monthly mean 550nm AOD from AERONET (black dots), MODIS (purple  
1425 triangles), MISR (red five-pointed stars) and the corresponding WRF-Chem simulation  
1426 (histogram) averaged for the period 2010-2014 at the East Asian sites, the Pacific island,  
1427 and the West U.S. sites as shown in Fig. 1.

1428

1429

1430

1431



1432

1433 **Figure 8** Seasonal mean EAE from the MODIS retrievals and the corresponding WRF-  
1434 Chem simulation averaged for the period 2010-2014, over the three sub-regions shown in  
1435 Fig. 4. The vertical bars represent 10<sup>th</sup> and 90<sup>th</sup> percentile values, the filled dots represent  
1436 the median values, and the triangles and circles represent the mean values.

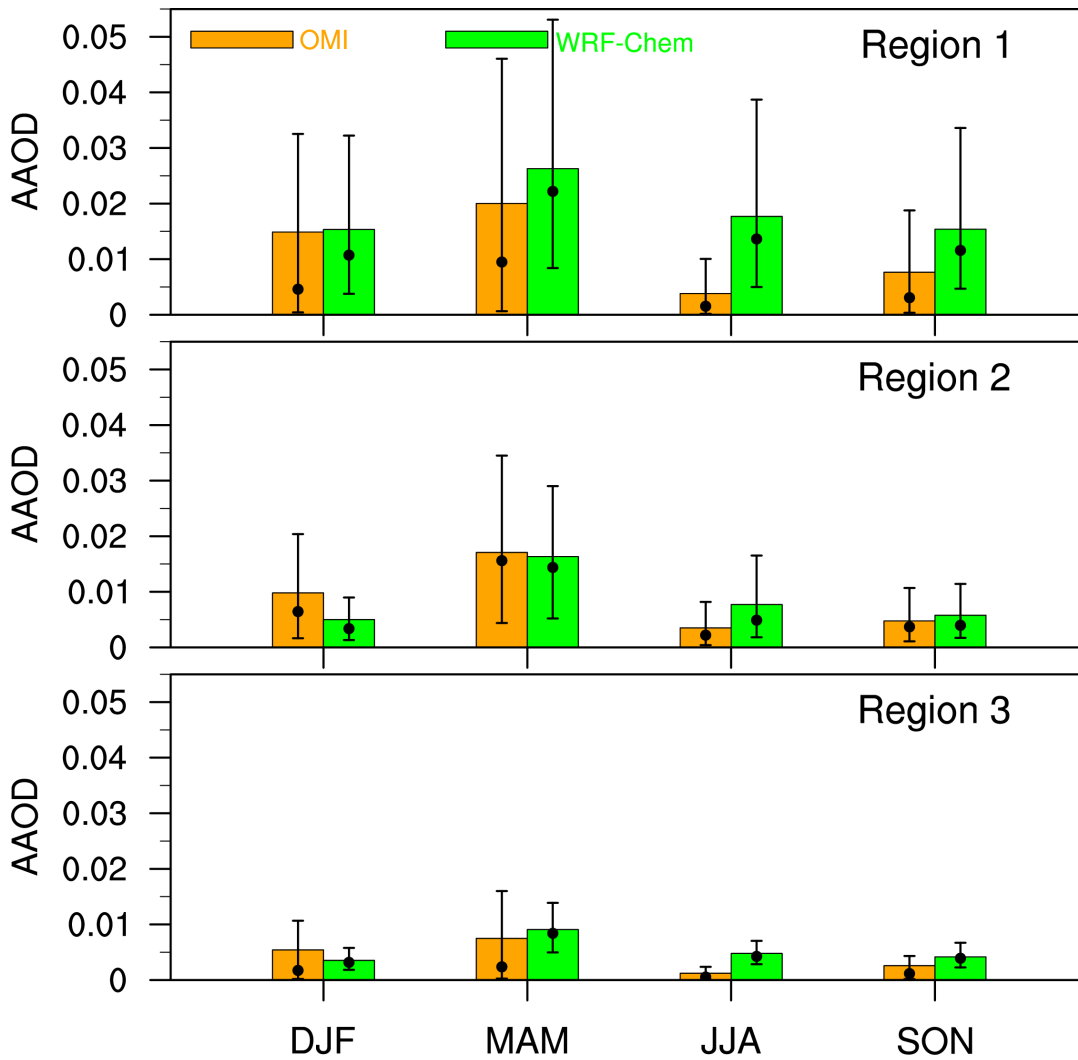
1437

1438

1439

1440

1441



1442

1443

1444

1445

1446

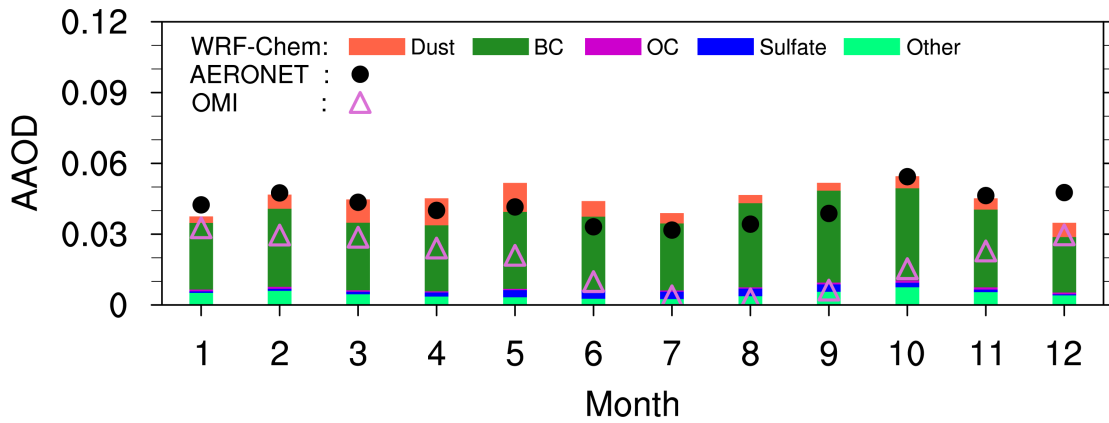
1447

1448

1449

**Figure 9** Seasonal mean AAOD at 500 nm from the OMI retrievals and the corresponding WRF-Chem simulation averaged for the period 2010-2014, over the three sub-regions shown in Fig. 4. The values of bars represent the mean. The vertical lines represent 10<sup>th</sup> and 90<sup>th</sup> percentile values, and the black dots represent the median values.

1450  
1451  
1452  
1453  
1454  
1455



1456  
1457  
1458  
1459  
1460  
1461  
1462  
1463  
1464  
1465

**Figure 10** Monthly AAOD from the retrievals of AERONET and OMI and the corresponding WRF-Chem simulation averaged for the period 2010-2014 over the East Asia sites as shown in Fig. 1.

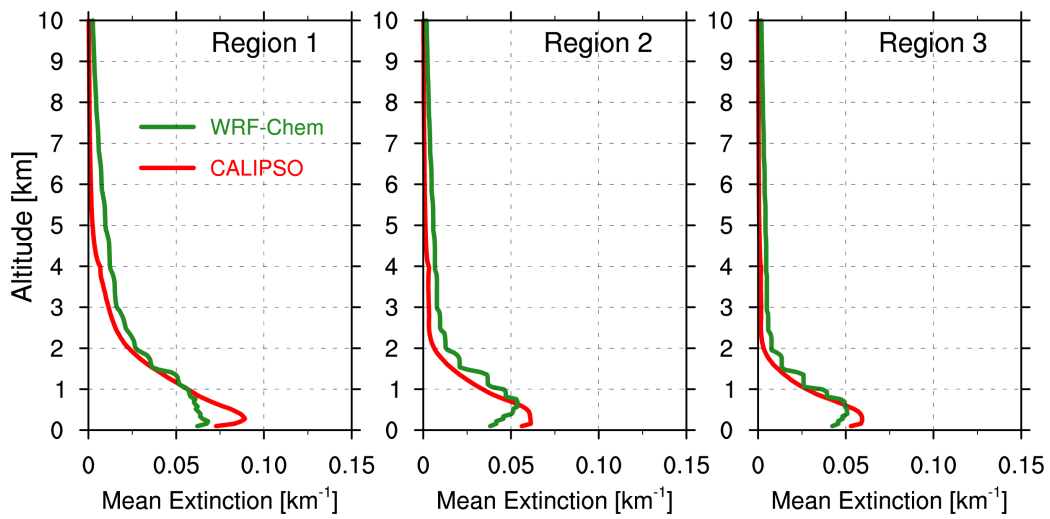
1466

1467

1468

1469

1470



1471

1472 **Figure 11** Annual vertical distributions of extinction from CALIPSO observations and  
1473 the corresponding WRF-Chem simulation averaged for the period 2010-2014 over the  
1474 three sub-regions shown in Fig. 4.

1475

1476

1477

1478

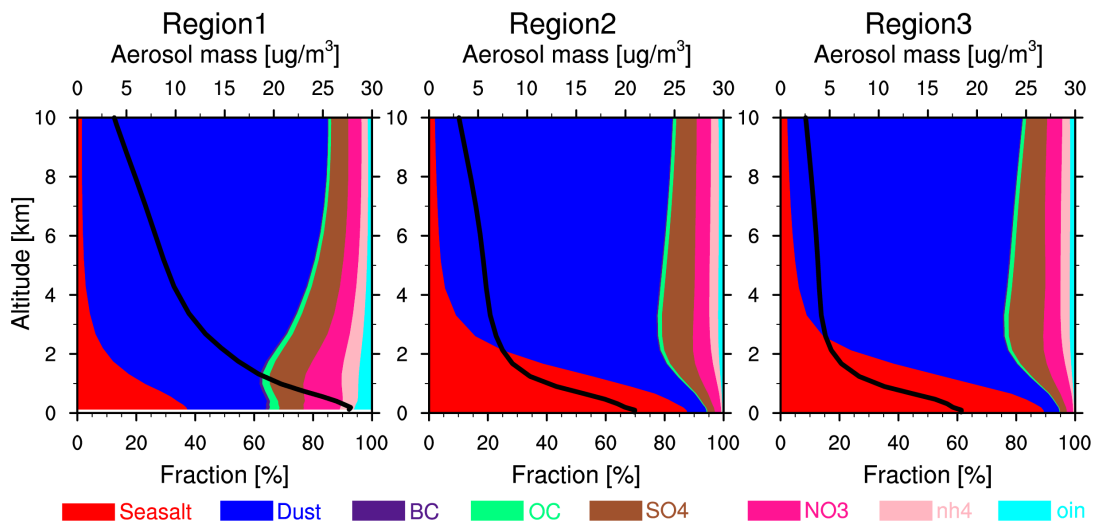
1479

1480

1481

1482

1483



1484

1485

1486

1487

1488

1489

1490

1491

1492

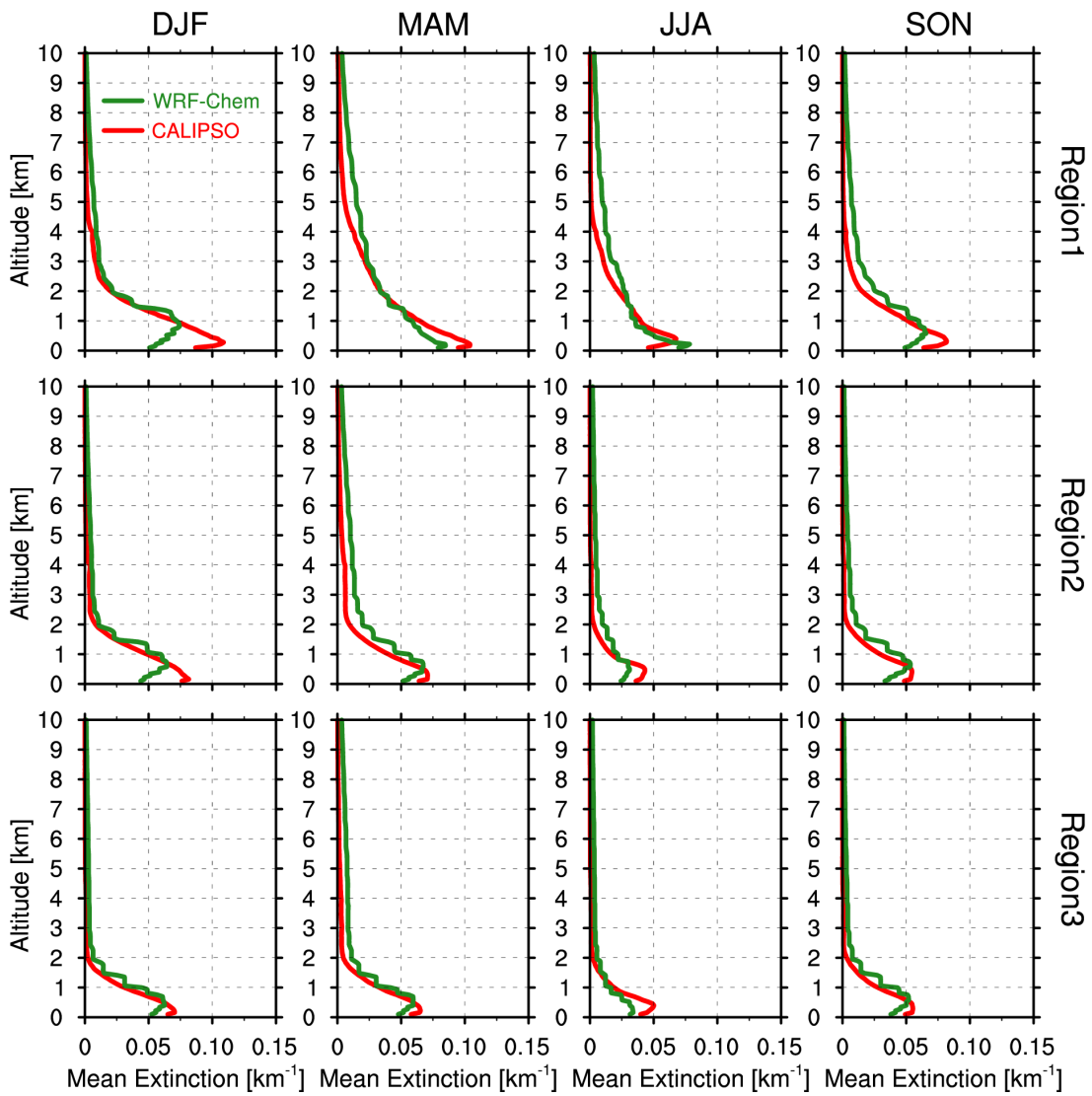
1493

1494

**Figure 12** Vertical distributions of mean aerosol mass (black solid line) and its composition fractions (colored shade-contour) from the WRF-Chem simulation averaged for the period 2010-2014 over three sub-regions as shown in Fig. 4.

1495

1496



1497

1498 **Figure 13** Vertical distributions of seasonal mean aerosol extinction from the CALIPSO

1499 retrievals and the corresponding WRF-Chem simulation averaged for the period 2010-

1500 2014 over three sub-regions as shown in Fig. 4.

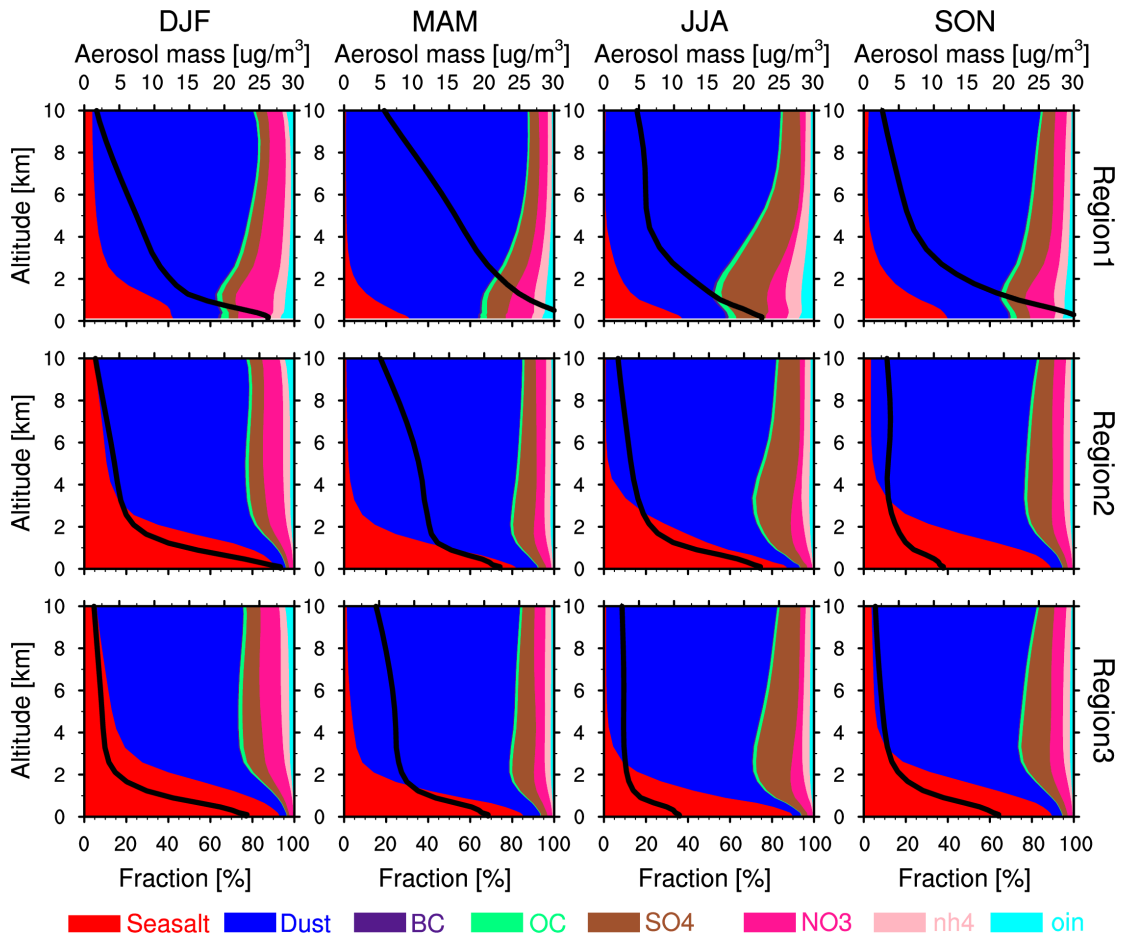
1501

1502

1503

1504

1505



1506

1507 **Figure 14** Vertical distributions of seasonal mean aerosol mass (black solid line) and its

1508 composition fraction (colored shade-contour) from the WRF-Chem simulation averaged

1509 for the period 2010-2014 over three sub-regions as shown in Fig. 4.

1510

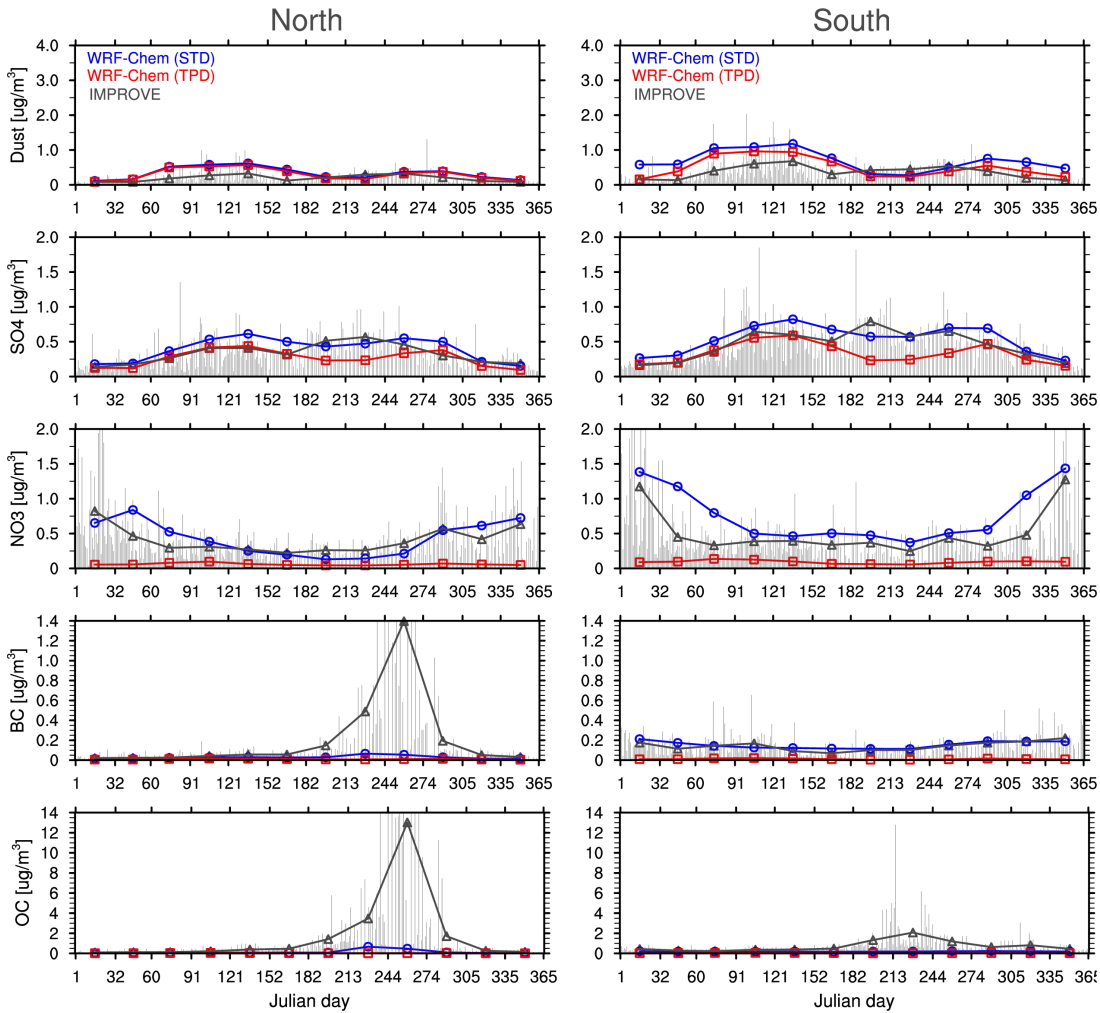
1511

1512

1513

1514

1515



1516

1517 **Figure 15** Daily mass concentrations of fine-mode ( $PM_{2.5}$ ) dust, sulfate, nitrate, BC, and

1518 OC averaged for the period 2010-2014 at the IMPROVE sites over the Northwest and

1519 Southwest U.S. (shown in Fig. 1) from the IMPROVE observations (vertical gray bars)

1520 and the monthly average of the IMPROVE observations (gray triangles) and the

1521 corresponding WRF-Chem standard simulation (STD; blue dots) and the sensitivity

1522 simulation without North American emissions (TPD; red dots).

1523